Celestial Mechanics and Dynamical Astronomy (2020) 132:3
https://doi.org/10.1007/s10569-019-9941-1

ORIGINAL ARTICLE

Effects of protoplanetary nebula on orbital dynamics of planetesimals in the outer Solar system

David Vokrouhlický[1] · **David Nesvorný**[2]

Received: 21 September 2019 / Revised: 10 November 2019 / Accepted: 29 November 2019

Abstract
Massive gaseous nebula has been a key element to formation of large solid objects (planetesimals, giant planet cores) in the early phase of the Solar system evolution. Here, we focus on its effects during the stage when giant planets have already fully formed. Dynamical effects of the nebula on motion of planetesimals stirred by planets were twofold: (i) global gravitational acceleration, and (ii) local aerodynamic drag. Thanks to decreasing gas density with radial distance, in the outer Solar system the effect of the drag was deemed to be important only for small planetesimals (sizes $\lesssim 10$ km). However, we find that it was possibly important up to the sizes of $\simeq 100$ km as well. The gravitational field of the nebula produces secular oscillations of the orbital eccentricity and inclination of planetesimals. Eventually, their pericenter may be lifted away from strong planetary influence, exhibited during close encounters, even for small bodies born in the planetary heliocentric zone. It has been previously suggested that such pathway may, in some nebula models, launch planetesimals onto large-inclination and small-eccentricity orbits in the trans-Neptunian region. These orbits would be dynamically stable to present epoch. Our simulations generally do not support such extreme cases, but we find that, after the nebula disperses, some planetesimals may indeed reach low-inclination and low-eccentricity orbits exterior to Neptune. These bodies may have been implanted into the Kuiper belt during subsequent planetesimal-driven migration of planets. This raises a possibility that some present-day KBOs may have formed in the giant-planet zone (5–20 au).

Keywords General · Solar nebula · Cosmogony · Origin and evolution · Gravitational fields · Orbital and rotational dynamics

This article is part of the topical collection on Trans-Neptunian Objects.
Guest Editors: David Nesvorny and Alessandra Celletti.

✉ David Vokrouhlický
vokrouhl@cesnet.cz

David Nesvorný
davidn@boulder.swri.edu

[1] Institute of Astronomy, Charles University, V Holešovičkách 2, 180 00 Prague 8, Czech Republic

[2] Department of Space Studies, Southwest Research Institute, 1050 Walnut St., Suite 300, Boulder, CO 80302, USA

Published online: 24 December 2019

1 Introduction

Formation of the Solar system is a center scientific problem in planetary science with various implications and lessons to be learned for exoplanetary systems. The general consensus indicates that it has been a drama at two acts. During act 1, giant planets, together with myriads of planetesimals up to roughly a moon size, formed and migrated within a massive gas nebula. Toward the end of this period, the gas dispersed. During act 2, solids were left on the scene. In the inner Solar system, terrestrial planets completed their formation. Outward, giant planets remained in an unstable configuration. This is because, as it is believed, much mass was still left in a vast sea of planetesimals roaming mainly beyond them. At some moment, gravitational effects of planetesimals started to push planets from their original orbs. Eventually, these processes triggered a short, but violent, phase of reorganization of planetary architecture and dispersal of most planetesimals, doping with them nearby interstellar space. As dictated by classical paradigms, through a subsequent phase of catharsis the Solar system then relaxed into its presently observed form.

How all this happened, and what were the main processes and steps toward the final result is a tremendously complex problem. In this situation, scientists necessarily seek to work with simplifications. As an example, researchers most often analyze the two formation acts separately (in fact, even the community of people working on act 1 is for the most part different from those working on act 2). This is possible, but only to some degree and only as an approximation. For instance, it is obvious that the first phase must smoothly connect to the second phase, or in other words, the initial conditions of the second phase are defined by terminal situation of the first phase. Indeed, modern variants of the second-phase studies already account for the fact that the giant planets leave the first phase—at all likelihood—in a mutually resonant configuration (e.g., Morbidelli et al. 2007; Nesvorný and Morbidelli 2012). It is also useful to remind that the whole giant task is an example of reverse engineering: knowing the present-day situation one infers what and how things happened in the past. Logically, the first phase encountered from this perspective in the second phase, only then followed by the first phase.

What we have at hand as a guide? Obviously, the final orbital architecture of planets. But this would not be restrictive enough, and we need more constraints to say useful things about the Solar system early evolution. Here, the analysis of nowadays stable, or quasi-stable, populations of small bodies in the Solar system becomes very valuable. This is because these small bodies represent a relic of planetesimals that once triggered the planetary instability. While for the most part lost, a tiny fraction of them was deposited into their present locations by interaction with orbitally evolving giant planets. As a result, parameters of the planetary migration left traces in number and orbital architecture of these populations of small Solar system bodies. So far these small-bodies-constraints were most often fruitfully applied when analyzing processes during the act 2 mentioned above (see Nesvorný 2018, and references therein). Overlaps into the act 1 in this respect were not studied extensively.

An interesting early work was conducted by Lemaitre and Dubru (1991). By studying location of secular resonances in the motion of test particles imposed by the present-day planetary configuration and the dispersing gas nebula, these authors attempted to seek explanation for excitation of eccentricities and inclinations observed for asteroids in the main belt. The concept is very interesting and in its essence survives to many forthcoming studies. It is worth mentioning that modern solution of this problem also has to do with processes in the first phase of the Solar system evolution as described by what is called "Grand-Track scenario" (Walsh et al. 2011). In this framework, the gravitational effect of the nebula plays

a minor role and all action is completed by migrating Jupiter and Saturn inward and outward throughout the whole range of the asteroid belt. Deposition of a small fraction of the planetesimals that survived in the asteroid zone till present was helped by the aerodynamics gas drag. The whole scenario explains the low mass of the asteroid belt, its compositional mixing, and potentially also details of the eccentricity and inclination distributions (see, e.g., Roig and Nesvorný 2015).

Raymond and Izidoro (2017) studied scattering of planetesimals, born in the heliocentric zone of Jupiter and Saturn, in a more conservative model, where Jupiter and Saturn had less spectacular migration histories. Even then, some planetesimals may evolve into the stable orbits by gas drag. These objects populate the outer main belt, where the asteroids of the appropriate spectral type C are located. During the scattering and deposition process, some of these planetesimals may also be accreted by terrestrial planets, which has relevance for their water content. Similarly, Brasser et al. (2007) studied whether aerodynamic gas drag may affect delivery of planetesimals into the inner Oort cloud zone when the Sun was still in its natal star cluster. Indeed, their results were positive, but indicated an interesting size-selective deposition efficiency: drag on small planetesimals ($\lesssim$ 5–10 km, say) was found too large and prevented their delivery to the Oort cloud. Its inner zone, if indirectly sensed via observations of large-perihelion comets in the future (e.g., Vokrouhlický et al. 2019), should thus be dominated by large bodies.

Another interesting study was presented by Kretke et al. (2012). Similar to study of Brasser et al. (2007), these authors considered outward scattering of planetesimals located in the giant-planet zone during the early stages of the Solar system evolution. However, instead of invoking aerodynamic gas drag they analyzed the effects of the gravitational field of the nebula. The gas drag was deemed to be negligible in their study because of (i) distant heliocentric zone, and (ii) large planetesimal sizes they investigated (in fact, we shall see below that this was only an approximation). In their model, planetesimals were able to decouple from the direct gravitational influence of giant planets by the gravitational effects of the nebula. Studying the efficiency of such decoupling, and the terminal orbits at which the planetesimals finally settled, Kretke et al. (2012) were able to predict whether these objects would be observable or not using available surveys. Interestingly, Kretke et al. (2012) were able to rule out cases when the nebula extended to large heliocentric distance, leaving plausible only models where the nebula had a cutoff at small heliocentric radii ($\lesssim$ 80 au, say). So while building on a negative result, from the deposition point of view, the method had an interesting predictive power.

Our initial plan was to (i) illustrate in more detail the underlying secular dynamical effects in Kretke et al. (2012), and (ii) extend their analysis which included only four-planet systems to five-planet models. We also realized that it would be useful to document in some depth how the gravitational potential, including its gradients (accelerations), of the nebula is computed. (Note, for instance, that the formula (34) in Brasser et al. (2007) is incorrect.) This is accomplished in Sect. 2. Next, Sect. 3 and on, we proceed with numerical simulations demonstrating orbital evolution of planetesimal population born in the giant-planet zone. We take into account planetary perturbations and gravitational accelerations of the gas nebula. In some of these simulations, we also include aerodynamic gas drag. After completing several runs similar to those in Kretke et al. (2012), we realized the results are not the same (see more discussion in Sect. 4.1). We find, instead, that the extended disk models cannot be ruled out as simply as presented in Kretke et al. (2012).

In addition, we were also interested in the planetesimal population left in the simulation after the nebula dispersal (either coupled or weakly decoupled from planets). This is because such planetesimal population, surviving from the gas-dominated phase of the Solar system evolution, was never implemented in the studies of the second phase, in which deposition

into stable small-body populations was studied. Typically, those studies assumed planetesimal source located exterior to planets and initially well-detached from them (e.g., Nesvorný 2018, for review. Interestingly, we shall see in Sect. 4.2 that the complementary planetesimal population available at the beginning of the second phase, and originating from the heliocentric zone among giant planets, may not be negligible when compared to that in the traditionally assumed exterior disk. This may have interesting implications for orbital behavior of planets during migration/instability and for implantation of bodies into the Kuiper belt and the Oort cloud.

2 Disk potential

Potential-density pairs for spherical and flattened configurations of mass have been extensively studied in Newtonian gravity (see, e.g., Binney and Tremaine 2008, Chap. 2). Particularly simple analysis concerns axially symmetric systems. In this case, the symmetry is associated with an azimuthal angle ϕ, which is consequently absent among the arguments of the density ρ and the potential function Φ. Depending on the choice of the coordinate system (cylindrical, spheroidal, etc.), the azimuthal angle is complemented with two additional coordinates u and v. Linearity of the Poisson's equation, and separability of the Laplace's operator in u and v, allows us to formulate Φ in terms of infinite series of fundamental (basis) solutions. A practical aspect of this approach consists in a possibility to truncate these series at low number of terms for often well-motivated density distributions. Analysis of very flat systems, such as we are interested in, however most often preclude this method, because series do not converge well.

Here, we choose the system of cylindrical coordinates, hence $u = R$ (radial coordinate) and $v = z$ (vertical coordinate). Both Φ and the density ρ are to be functions of R and z only. Additionally, the simplest, yet useful, studies of protoplanetary nebula motivate models of flat disks with exponential [$\propto \exp(-|z|/z_{\rm s})$] or Gaussian [$\propto \exp(-(z/z_{\rm s})^2)$] vertical profiles of ρ characterized with a scale height $z_{\rm s}$ (e.g., Hayashi 1981; Hayashi et al. 1985). Earn (1996) developed an interesting method tailored to the case of disks with such exponential vertical profiles (compare also with Binney and Tremaine 2008, Chap. 2.6.2). The resulting formula for the potential Φ is expressed using a single integration only, provided the radial density distribution has a simple, analytic form of its Hankel transform (otherwise, a second integration is needed for its determination). Unfortunately, truncated power-law disks, such as assumed in protoplanetary studies, do not allow the former. Additionally, the scale height is often not constant, but typically increases with R. In this situation, we take a more laborious but straightforward path, in which the disk potential Φ—for a pre-defined density distribution ρ—is expressed as a double integral over R and z directly. It can be understood as a composition of contributions from infinitesimal rings at a vertical location z and with radius R.

2.1 Model with a Gaussian vertical profile

Assume an axisymmetric disk with gas density distribution

$$\rho\,(r,z) = \rho_0\, r^{\alpha}\, \exp(-z^2/z_{\rm s}^2)\;, \tag{1}$$

where r and z are cylindrical radial and vertical coordinates (given in au, while ρ_0 has a unit of density). Henceforth, the radial profile is characterized by a power-law exponent $\alpha < 0$,

and the vertical profile is Gaussian with a scale height z_s, possibly depending on the radial distance

$$z_s(r) = z_0\, r^{\beta} \tag{2}$$

($\beta \geq 0$ indicates the disk become thicker at larger distance from the center). Here α, β and z_0, together with ρ_0, are free parameters of the model, possibly also time dependent. This simple model dates back to Hayashi (1981), see also Hayashi et al. (1985), and it was used for instance in Brasser et al. (2007). The nominal values of the parameters chosen for the canonical minimum mass Solar nebula are $\alpha = -11/4$, $z_0 = 0.047$, $\beta = 5/4$ and $\rho_0 = 1.4 \times 10^{-6}$ kg/m^3 (e.g., Weidenschilling 1977a; Hayashi 1981). Here, the disk is assumed to have inner and outer boundaries at $r = R_i$ and $r = R_o$, respectively. One easily verifies that the total mass M of the nebula is

$$M = \frac{\pi^{3/2}}{\gamma}\, M_0\, z_0 \left(R_o^{2\gamma} - R_i^{2\gamma}\right) , \tag{3}$$

where $\gamma = 1 + (\alpha + \beta)/2$ (with the nominal values mentioned above $\gamma = 1/4$) and M_0 is a mass of au^3 with density ρ_0. When $\gamma = 0$, the mass M is simply $M = 2\pi^{3/2}\, M_0\, z_0 \ln(R_o/R_i)$. Using the nominal values of the model constants, one obtains nebular mass of a few percents of the solar mass with R_o between 30 and 100 au (e.g., Hayashi 1981). Often reported is also the surface density $\Sigma(r)$ of the disk model. In our case,

$$\Sigma(r) = \int_{-\infty}^{\infty} \rho(r, z)\, \mathrm{d}z = \sqrt{\pi}\, \rho_0\, z_0\, r^{\alpha+\beta} . \tag{4}$$

Again, for parameters having their nominal values cited above one has $\sqrt{\pi}\, \rho_0\, z_0 \simeq 1750\,\mathrm{g/cm^2}$ and $\alpha + \beta = -3/2$.

Gravitational potential $\Phi(r, z)$ of the disk source with the density distribution described above cannot be given analytically. A straightforward approach is to represent $\Phi(r, z)$ using a superposition of potentials corresponding to infinitesimal rings of radii $R \in (R_i, R_o)$ and vertical location $Z \in (-\infty, \infty)$. Note that the mirror symmetry in z of the density implies a respective symmetry of the potential $\Phi(r, z)$. However, choosing a location (r, z) still requires a superposition of contribution of the source rings with Z spanning all values between $-\infty$ to ∞. The potential $\Phi_r(r, z)$ of a ring may be found in an analytical form, e.g., in Lass and Blitzer (1983) or Binney and Tremaine (2008). Assuming its total mass M_r, we have

$$\Phi_r(r, z) = \frac{G M_r}{\pi \sqrt{rR}}\, k_- \mathbf{K}(k_-) , \tag{5}$$

where G is gravitational constant, $\mathbf{K}$ is the complete elliptic integral of the first kind, and modulus k_- is given in Eq. (8).

The above-mentioned superposition must be performed numerically. To that goal, it is useful to fold the Z coordinate onto a finite domain using some new variable t. Then, a straightforward algebra provides $\Phi(r, z)$ in a form of a double integral

$$\Phi(r, z) = \frac{\pi \Phi_0}{\sqrt{r}} \int_{R_i}^{R_o} \mathrm{d}R\, R^{\alpha+1/2}\, z_s(R) \int_0^1 \frac{\kappa(t, R)\, t\, \mathrm{d}t}{\sqrt{-\ln(1 - t^2)}} , \tag{6}$$

where Φ_0 is a potential of point mass M_0 at a distance of one astronomical unit, and hence $\Phi_0 = -GM_0/r_0$ ($r_0 = 1$ au). The inner kernel $\kappa(t, R)$ is

$$\kappa(t, R) = \frac{2}{\pi} \left[k_+ \mathbf{K}(k_+) + k_- \mathbf{K}(k_-)\right] . \tag{7}$$

The complete elliptic integral of the first kind **K** appears here with two moduli

$$k_{\pm} = 2\sqrt{\frac{r\,R}{(r+R)^2+(z\pm Z)^2}}\ , \tag{8}$$

with the vertical source coordinate Z given by $Z(t) = z_{\rm s}\sqrt{-\ln(1-t^2)}$. The choice of t suitably regularizes the second integration, but a care must still be paid to the integral over the radial coordinate R when r is within the disk boundaries. This is because the modulus k_- becomes unity when $z = Z$ and $r = R$. The value of the complete elliptic integral $\mathbf{K}\,(k_-)$ then diverges, with obviously a finite value of the resulting potential $\Phi(r,z)$. Such an integrable singularity in the integrand of (6) may be regularized by splitting the integration over R to segments from $R_{\rm i}$ to r and from r to $R_{\rm o}$, and in both cases perform a standard coordinate transformation described for instance in Press et al. (2007).

2.2 Model with a non-Gaussian vertical profile

The Gaussian vertical profile in the gas density (1) corresponds to the simplest assumption of the (locally) isothermal and optically thin disk. With more involved equations of state, it may become more complicated, in particular more slowly decreasing from the disk midplane. To test whether this has importance for our results, and to directly compare our results with relevant previous studies, we also used disk models from Kretke et al. (2012) that have

$$\rho\,(r,z) = \rho_0\,r^{\alpha}\,\exp(-|z|/z_{\rm s})\ , \tag{9}$$

with r and z again being the cylindrical radial and vertical coordinates. Unlike in Kretke et al. (2012), who assume constant scale height $z_{\rm s}$, we generally adopt the flaring disk model with $z_{\rm s}$ given by Eq. (2) and $\beta \simeq 5/4$. Disk mass with inner and outer boundary at $r = R_{\rm i}$ and $r = R_{\rm o}$, respectively, is now

$$M = \frac{2\pi}{\gamma}\,M_0\,z_0\left(R_{\rm o}^{2\gamma} - R_{\rm i}^{2\gamma}\right)\ , \tag{10}$$

with $\gamma = 1+(\alpha+\beta)/2$ as above ($\gamma = 0$ case has $M = 4\pi\,M_0\,z_0\ln(R_{\rm o}/R_{\rm i})$). The surface density $\Sigma(r)$ of this disk model now reads

$$\Sigma(r) = 2\,\rho_0\,z_0\,r^{\alpha+\beta}\ . \tag{11}$$

Gravitational potential of the disk with bulk density distribution (9) can be expressed using the same approach as above. We obtain

$$\Phi\,(r,z) = \frac{\pi\,\Phi_0}{\sqrt{r}}\int_{R_{\rm i}}^{R_{\rm o}} {\rm d}R\,R^{\alpha+1/2}\,z_{\rm s}\,(R)\int_0^1 \kappa\,(t,R)\,{\rm d}t\ , \tag{12}$$

with the kernel function still as in Eq. (7), but now the Z coordinate of the contributing ring be $Z(t) = -z_{\rm s}\,\ln t$.

Note that any of the density distribution parameters, as well as the inner and outer disk boundaries, may be time dependent, imposing thus the corresponding time dependence of the potential $\Phi(r,z)$. The disk may also be a composition of radial segments having different values of inner and outer boundaries. Its potential will still be given with a superposition of terms similar to Eq. (6) or (12) with corresponding lower and upper limits in the integration over R.

2.3 Validation of the code

The above presented expressions for the disk potential (6) and (12) were programmed using standard Romberg method (e.g., Press et al. 2007). The complete elliptic integrals in the kernel (7) are efficiently expressed using the Jacobian elliptic integrals represented with fast-converging series. Before using them in our simulations, we sought a possibility both to validate the formulas above and to identify/prevent any programming errors.

The simplest level of justification, basically verifying normalization factors in (6) and (12), is to compare the potential to $-GM/\sqrt{r^2+z^2}$ function at a large distance from the center, namely a potential of point-source with the total disk mass M (given in Eq. 3 or 10). However, this is too easy for an in-depth check. Therefore, we sought more stringent tests, where we would compare results from our numerical code against analytical potential-density pairs for axisymmetric sources.

Uniform disk Our first example is a gravitational potential Φ of a finite, uniform and two-dimensional (2D) disk with radius R and a constant surface density Σ_0. Lass and Blitzer (1983) provided an analytic form

$$\Phi(r,z) = 2G\Sigma_0\Bigg[\pi\,|z|\,H_1(R-r) - B\,\mathbf{K}(k) - \frac{R^2-r^2}{B}\mathbf{E}(k) - \frac{R-r}{R+r}\frac{z^2}{B}\mathbf{\Pi}\left(n^2,k\right)\Bigg], \tag{13}$$

where $\mathbf{K}$, $\mathbf{E}$ and $\mathbf{\Pi}$ are the complete elliptic integrals of the first, second and third kind, respectively (e.g., Byrd and Friedman 1971). Their modulus and characteristic read

$$k = \frac{2\sqrt{Rr}}{B}\,, \quad n^2 = \frac{4Rr}{(R+r)^2}\,, \tag{14}$$

with

$$B^2 = (R+r)^2 + z^2\,. \tag{15}$$

Note we use a standard Legendre form of the elliptic integrals in Byrd and Friedman (1971). Attention must be paid, in particular, to the sign of the characteristic n^2, which differs from that in Press et al. (2007). The potential has a global minimum value $\Phi_0 = -2\pi G\Sigma_0 R = -2GM/R$ in the center of the disk (here M stands for its total mass), and it offers a suitable normalization $\Phi' = \Phi/|\Phi_0|$. The presence of the Heaviside function $H_1(x)$ in the right-hand side of Eq. (13) means that the first term in the bracket applies only when $r < R$; otherwise, it is zero.

Partial derivatives of Φ, thus the acceleration components, may also be expressed in a closed form (see the Appendix in Vokrouhlický and Karas 1998)

$$\frac{\partial\Phi}{\partial r} = -\frac{2G\Sigma_0}{rB}\left[B^2\mathbf{E}(k) - \left(R^2+r^2+z^2\right)\mathbf{K}(k)\right], \tag{16}$$

and

$$\frac{\partial\Phi}{\partial z} = 2G\Sigma_0\left\{\pm\pi\,H_1(R-r) - \frac{z}{B}\left[\mathbf{K}(k) + \frac{R-r}{R+r}\mathbf{\Pi}\left(n^2,k\right)\right]\right\}. \tag{17}$$

Because of their nature, a suitable normalization factor of the partials is Φ_0/R. As again signaled by the presence of the Heaviside function, the first term $\pm\pi$ in the bracket of the right-hand side of Eq. (17) applies only when $r < R$ and the negative sign for $z < 0$, while the positive sign for $z > 0$; otherwise, this term is zero. Discontinuity in the potential derivatives $\partial\Phi/\partial z$ in the direction normal to the disk plane is the property of the 2D model. Recall that

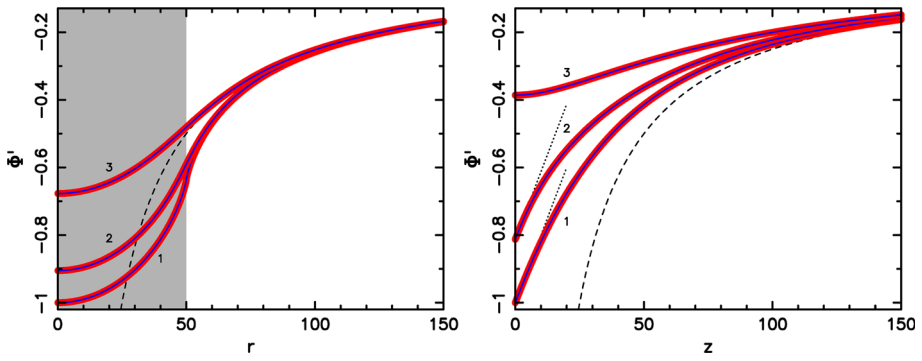

Fig. 1 Normalized potential $\Phi' = \Phi/|\Phi_0|$ of a uniform disk with radius $R = 50$ (arbitrary units). Left: Solid lines for three values of the fixed z coordinate (r at the abscissa); $z = 0$ (label 1), $z = 5$ (label 2), and $z = 20$ (label 3). Red curves computed numerically using Eq. (12) with $\alpha = \beta = 0$ (uniformity of the surface density), $R_\mathrm{i} = 0$ and $z_0 = 0.001$ (very thin disk approximating the 2D model of Lass and Blitzer 1983). Blue curves computed using the analytic formula (13). Dashed and black line is a potential of a point-source with a mass M of the disk. The gray shade area indicates location of the disk. Right: Solid lines for three values of the fixed r coordinate (z at the abscissa); $r = 0$ (label 1), $r = 40$ (label 2), and $r = 70$ (label 3). Red curves computed numerically using Eq. (12) with parameters as above ($\alpha = \beta = R_\mathrm{i} = 0$ and $z_0 = 0.001$). Blue curves computed using the analytic formula (13). Dashed and black line is a potential of a point-source with a mass M of the disk. Dotted lines at curves 1 and 2 have a slope $2GM/R^2$, as required by (17) in the region of the mass source ($r < R$); outside the disk zone (curve 3), the slope is zero

on an oriented infinitesimally thin slab with normal direction $\mathbf{n}$ and surface density Σ, the potential Φ gradient has a discontinuity (e.g., Binney and Tremaine 2008)

$$[\mathbf{n} \cdot \nabla\Phi]_\pm = \pm 2\pi\, G\, \Sigma\ . \tag{18}$$

In our case, $\mathbf{n}^T = (0, 0, 1)$ and $r < R$, which delimits the source region. In the full three-dimensional (3D) model, the midplane partial derivative with respect to z is obviously zero owing to the symmetry of the potential under the mirror transformation $z \to -z$.

Since our disk model in Sects. 2.1 or 2.2 is 3D with an exponential decrease in the z direction, we approximate the thin disk case by considering suitably small value of the scale height z_s. For the sake of our test, we took $z_0 = 0.001$ and $\beta = 0$ (no flaring). Uniformity of the surface density then requires $\alpha = 0$, and to conform the finite disk case of Lass and Blitzer model we had $R_\mathrm{i} = 0$ and $R_\mathrm{o} = R$. We could have taken any of the expressions (6) or (12) corresponding to Gaussian or non-Gaussian vertical density profiles; we took the second case.

Figure 1 shows a comparison of our numerically determined potential at several fixed values of z (left) and r (right) coordinate with the analytical value from Eq. (13). The match is fairly good. The same applies also to a comparison of the partial derivatives of the potential shown in Fig. 2. In order to compute the partials numerically, we determine potential values at neighbor values of the coordinate and use three-point formula. When computing the derivative at the central point, it simplifies to $\partial\Phi(r,z)/\partial r \simeq [\Phi(r+h_\mathrm{r},z) - \Phi(r-h_\mathrm{r},z)]/2h_\mathrm{r}$ and $\partial\Phi(r,z)/\partial z \simeq [\Phi(r,z+h_\mathrm{z}) - \Phi(r,z-h_\mathrm{z})]/2h_\mathrm{z}$. We used $h_\mathrm{r} = 0.05$ and $h_\mathrm{z} = 0.1$, the same values as we also used for our orbital integrations below. The radial derivative is singular at the edge of the disk in its plane (this is because $k \to 1$ in the argument of the complete elliptic integral of the first kind in the right-hand side of Eq. 16). The vertical derivative has only a discontinuity related to the first term of Eq. (17); note the corresponding elliptic integral is now multiplied by z, which helps to regularize this term.

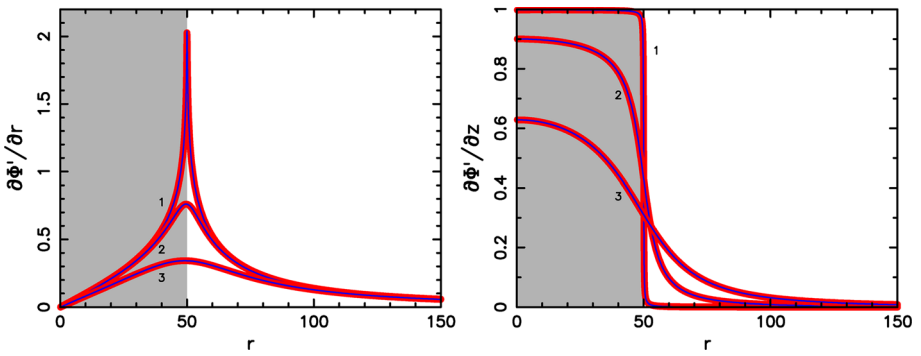

Fig. 2 Partial derivative with respect to cylindrical r (left) and z (right) coordinates of a uniform disk potential Φ normalized with $\Phi_0/R = -2GM/R^2$ (M is total mass of the disk and R its radius; the same parameters as in Fig. 1 used). On both panels, the derivatives are computed for three values of the fixed z coordinate (r at the abscissa); $z = 0.05$ (label 1), $z = 5$ (label 2), and $z = 20$ (label 3). The numerically computed derivatives use a three-point interpolation formula of the potential values (the same as in our orbital code). Red curves computed numerically, blue curves using the analytic formulas (16) and (17). The radial derivative is singular in the disk plane ($z = 0$) and at the edge of the disk $r = R$. The vertical derivative has a discontinuity at the same point. The gray shade area indicates location of the disk

Kuzmin disk An amazingly simple disk-potential pair has been discovered by Kuzmin (1956) (see also Binney and Tremaine 2008). It consists again of an infinitesimally thin 2D disk with surface density profile

$$\Sigma(r) = \frac{M}{2\pi}\frac{a}{(a^2+r^2)^{3/2}}\ , \tag{19}$$

with a potential

$$\Phi(r,z) = -\frac{GM}{\left[r^2+(a+|z|)^2\right]^{1/2}}\ . \tag{20}$$

Here, a is an arbitrary scaling parameter and M is the total mass of the disk. The disk is infinite, with no boundaries ($R_\mathrm{i} = 0$ and $R_\mathrm{o} = \infty$). Partial derivatives of the potential are therefore also trivial to be expressed, namely

$$\frac{\partial\Phi}{\partial r} = \frac{GMr}{\left[r^2+(a+|z|)^2\right]^{3/2}}\ , \tag{21}$$

and

$$\frac{\partial\Phi}{\partial z} = \pm\frac{GM\,(a+|z|)}{\left[r^2+(a+|z|)^2\right]^{3/2}}\ , \tag{22}$$

with the sign plus applying for $z > 0$ and vice versa. As in the case of the uniform finite disk above, $\partial\Phi/\partial z$ has a discontinuity at the disk plane $z = 0$ to obey Eq. (18). The value at the center of the disk, namely $r = z = 0$, $\Phi_0 = -GM/a$ provides again a natural normalization factor for the potential $\Phi' = \Phi/|\Phi_0|$. Because the disk is now infinite, the only scale length is the parameter a and thus partials Eqs. (21) and (22) have a logical normalization factor Φ_0/a.

Figures 3 and 4 show comparison between the numerically and analytically computed potential and its partial derivatives for a Kuzmin disk with $a = 25$. In the numerical settings, we used vertical scale height $z_0 = 0.001$ (and $\beta = 0$), and inner and outer disk boundaries

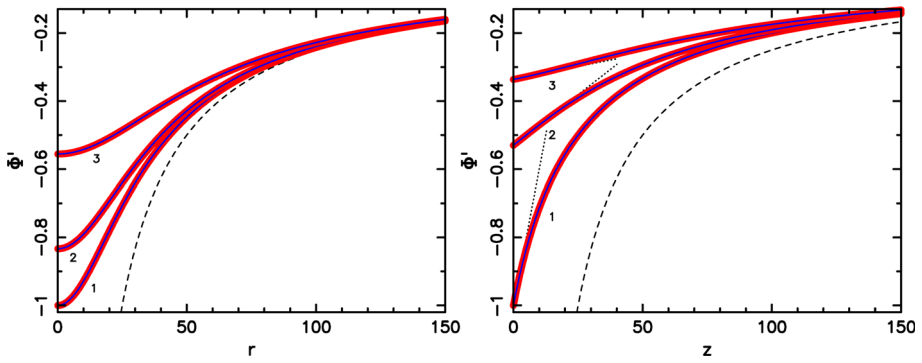

Fig. 3 Normalized potential $\Phi' = \Phi/|\Phi_0|$ of a Kuzmin disk with a scale parameter $a = 25$ (arbitrary units). Left: Solid lines for three values of the fixed z coordinate (r at the abscissa); $z = 0$ (label 1), $z = 5$ (label 2), and $z = 20$ (label 3). Red curves computed numerically using Eq. (12) with $\alpha = \beta = 0$, $R_\mathrm{i} = 0$, $R_\mathrm{o} = 10^5$ and $z_0 = 0.001$ (very thin disk approximating the 2D Kuzmin model). Blue curves computed using the analytic formula (20). Dashed and black line is a potential of a point-source with a mass M of the disk. Right: Solid lines for three values of the fixed r coordinate (z at the abscissa); $r = 0$ (label 1), $r = 40$ (label 2), and $r = 70$ (label 3). Red curves computed numerically using Eq. (12) with parameters as above ($\alpha = \beta = R_\mathrm{i} = 0$, $R_\mathrm{o} = 10^5$ and $z_0 = 0.001$). Blue curves computed using the analytic formula (19). Dashed and black line is a potential of a point-source with a mass M of the disk. Dotted lines at curves 1, 2 and 3 have a slope expressing discontinuity of the partial derivative $\partial\Phi/\partial z$ from (18)

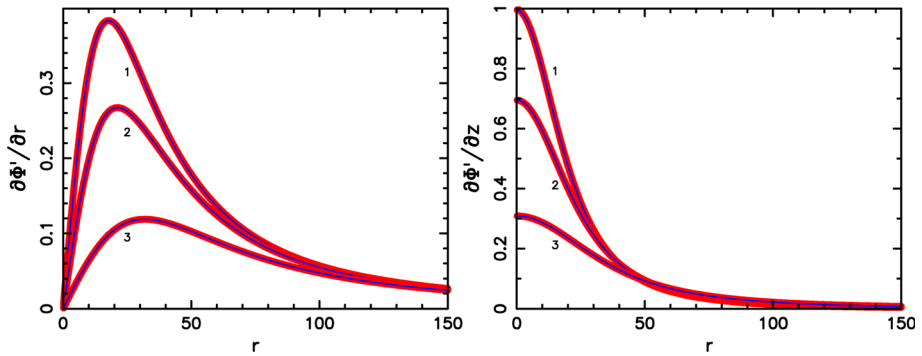

Fig. 4 Partial derivative with respect to cylindrical r (left) and z (right) coordinates of a Kuzmin disk potential Φ normalized with $\Phi_0/a = -GM/a^2$ (M is total mass of the disk, and a its scale parameter; the same parameters as in Fig. 3 used). On both panels, the derivatives are computed for three values of the fixed z coordinate (r at the abscissa); $z = 0.05$ (label 1), $z = 5$ (label 2), and $z = 20$ (label 3). The numerically computed derivatives use a three-point interpolation formula of the potential values (the same as in our orbital code). Red curves computed numerically, blue curves using the analytic formulas (21) and (22)

$R_\mathrm{i} = 0$ and $R_\mathrm{o} = 10^5$. In this case, we replaced R^α factor in the integrand of Eq. (12) with $a\,(a^2 + R^2)^{-3/2}$, as required by the surface density (19).

3 Numerical setup

Results presented in the previous section allowed us to gain a confidence in our modeling of the disk gravitational potential and the corresponding accelerations. Next, we briefly outline

our tools used for numerical propagation of planetesimal orbits with a combined perturbative effect from planets and the nebula.

3.1 General tools and approach

We used `swift_rmvs4` code, part of the `swift`-family software, which allows users an efficient propagation of N massive (the Sun and planets) and M massless bodies (small planetesimals). In this setup, the structure of the integrator implements symplectic map first developed by Wisdom and Holman (1991) and it allows to consistently propagate heliocentric motion of planets, accounting for their mutual gravitational perturbations, and motion of massless particles under the gravitational effect of the Sun and planets. Given our goals, we extended the integrator by the effects of the gaseous protoplanetary disk on massless planetesimals in two respects: (i) its gravitational acceleration, and (ii) drag effects.

As to the gravitational effect of the nebula, we precomputed its potential using formulas given in Sects. 2.1 and 2.2 on a large and dense grid of points. In particular, we used 0–300 au range in both r and z coordinates with steps 0.05 and 0.1 au, respectively (see out tests in Sect. 2.3). Owing to the mirror symmetry of the potential about the disk plane, assumed to coincide with planetary orbital planes, we may use only positive z values. This resulted in an output table of a still acceptable 740 MB size. Accelerations due to the disk potential are then computed as in Sect. 2.3, with interpolation of the potential within the gridpoints using the three-point formula.

In some of our simulations, we also implemented the aerodynamic drag due to the nebular gas. To that end, we used the approach outlined in Sec. 2 of Brasser et al. (2007) (see also Weidenschilling 1977b). The drag acceleration is

$$\mathbf{a}_{\rm D} = -\frac{3}{4}\frac{C_{\rm D}}{D}\frac{\rho}{\rho_{\rm p}} v_{\rm r}\mathbf{v}_{\rm r} \,, \tag{23}$$

where ρ is the gas volume density from either Eq. (1) or (9), $\rho_{\rm p}$ and D are the bulk density and the size of a planetesimal (assumed spherical), $\mathbf{v}_{\rm r}$ is the relative velocity with respect to the gas. Note the latter is composed of the planetesimal heliocentric velocity and gas velocity, which is assumed circular and slightly sub-Keplerian thanks to the pressure support (e.g., Weidenschilling 1977b; Brasser et al. 2007). Finally, $C_{\rm D}$ is the dimensionless aerodynamic drag coefficient. For highly supersonic regime, $C_{\rm D}$ approaches a limiting value of 2; otherwise, $C_{\rm D}$ is a rather complex function of the Mach's and Reynolds' numbers as described in Brasser et al. (2007). In the swift architecture, we implemented the disk-related accelerations as an outer shell to the code propagation of planets and particles due to the planetary effects. We use simple, first-order leap-frog method.

Note that none of these accelerations is applied to planets. This is because our simple approach neglects details that would have been necessary to properly model these effects. First, we disregard cavities in the disk within 2–3 Hill radii distance around their orbits. This basically halts the drag effect on them. The issue of gravitational effect of the nebula on planets is of a more delicate nature. This perturbation exists, but is related to the torques raised by non-axisymmetric spiral arms launched by the planets on the disk density distribution. Our axisymmetric model is not able to express these effects. However, we effectively account for them by assuming a stable resonant architecture of the planets (to which the disk gravity contributes). So we only disregard the fine disk structures, such as planet-related cavities and density non-axisymmetric arms, when modeling the nebular effects on the motion of planetesimals. Modeling of such details is well beyond the scope of this paper.

Each of our integrations spanned 10 Myr and used 0.1 yr timestep. State vectors, heliocentric positions and velocities, of planets and planetesimals were exported every 10 kyr for further analysis. The gas density is assumed to exponentially decay with a characteristic timescale of 2 Myr (for context, see, e.g., Kretke et al. 2012). Therefore, at the end of each of our simulations, the gas density drops to less then 0.7% of its initial value. In each of the tested cases, the system then transits to planet-dominated phase. We ran a limited set of simulations with even shorter decay timescale of 1 Myr, but our main conclusions were not affected. In each of our runs, the time evolution of the disk density is global without changing any other of its parameters (such disk boundaries, or characteristic exponents of its radial profile). We did not attempt to explore more complicated situations where also the inner (R_i) or outer (R_o) disk radii would dynamically evolve, for instance due to photoevaporation due to central or outer stars in the birth cluster (e.g., Alexander et al. 2006).

3.2 Initial setup

The planetary system we propagate consists of the giant planets only. They are assumed to be already fully formed, but their orbits differ from their current architecture. Following studies of giant-planet-core growth and migration in the earliest phases of the protoplanetary disk evolution (e.g., Masset and Snellgrove 2001; Morbidelli et al. 2007, and references therein), we assume a resonant configuration of planets. For the sake of comparison, we consider two sets of simulations.

In the first case, we assume four giant planets in the heliocentric order taken from the current Solar system. Some of their resonant configurations were tested by Morbidelli et al. (2007). We selected one of the long-term stable resonant configurations, in which Jupiter up to Neptune are consequently locked in 3:2, 3:2 and 4:3 mean-motion resonances. Jupiter's mean semimajor axis is $\simeq 5.43$ au, and Neptune is at $\simeq 11.61$ au. Their orbits are initially coplanar and near-circular. Throughout our 10 Myr lasting simulations, the planetary configuration remained stable. Obviously, at later stages the gravitational effect of the planetesimals located exterior to the planets will destabilize the planetary initial compact configuration and will lead through radial migration and chaotic reconfiguration toward the current architecture of the Solar system. This later phase is not modeled in our work.

In the second case, we assume an initial configuration of five giant planets (the observed planets plus an additional ice giant in between Saturn and Uranus, e.g., Nesvorný 2011; Batygin et al. 2012; Nesvorný and Morbidelli 2012). It has been argued that such systems have higher chances to reproduce the final planetary system. The loss of the third ice giant, by mutual scattering with Jupiter, absorbs the most violent element of the planetary reconfiguration phase, giving more changes for the remaining planets to settle onto their regular, final orbits. Our five-planet system has been selected from those tested by Nesvorný and Morbidelli (2012). It represents a resonant chain of near-circular and coplanar orbits in mean-motion resonance chain 3:2, 3:2, 2:1 and 3:2. With those parameters, Jupiter has an initial semimajor axis $\simeq 5.59$ au and Neptune is at $\simeq 22.52$ au. As before, the planets remain stable through our simulation.

In each of our runs, we used 30,000 planetesimals distributed initially among the planetary orbits (their innermost orbits have semimajor axis by 0.5 au smaller than Jupiter, while the outermost orbits have semimajor axis by 0.5 au larger than Neptune in the chosen planetary set). To prevent unwanted, large population of planetary coorbitals, we avoided planetesimal semimajor axis values within the 0.25 Hill distance from planetary orbits. The eccentricity and inclination initial values were drawn randomly from a Rayleigh distribution with a small

Table 1 Summary of disk parameters used in our first set of simulations: surface density at 1 au heliocentric distance $\Sigma_0 = 2000$ g/cm^2, inner radius $R_i = 1$ au, exponential vertical profile from Sect. 2.2 with a constant scale height $z_0 = 0.05$ au ($\beta = 0$), and two power-indexes of the surface density profile $\alpha = -1.5$ (left column) and $\alpha = -1$ (right column)

R_o (au)	$\alpha = -1.5$	$\alpha = -1$
30	1.27/13.3	4.10/ 42.9
40	1.51/15.8	5.51/ 57.8
50	1.72/18.0	6.93/ 72.6
60	1.91/20.0	8.34/ 87.4
80	2.25/23.5	11.17/117.0
100	2.55/26.7	14.00/146.6

Rows for different values of the outer disk radius R_o between 30 and 100 au. The body of the table provides mass of the disk M in percents of the solar mass and in mass of Jupiter (the first and the second inputs, respectively)

scale parameter of 0.01 in eccentricity and 0.3° in inclination. Secular angles, as well as the longitude in orbit, were selected randomly. Planetesimals were removed during the simulation when they impacted one of the massive bodies (the Sun, modeled with an enlarged radius of 0.05 au, or the planets, for which we used their true radii), or when their positions appeared to be beyond the precomputed 300 × 300 au^2 grid in cylindrical r and z coordinates (or, roughly, when they exceeded 300 au heliocentric distance).

In a limited set of runs, we also considered planetesimals located in a disk exterior to the outermost planet up to 50 au heliocentric distance. We verified, but do not report here in detail, that except for innermost particles at a few Hill radii distance from the orbit of Neptune the disk remained unperturbed.

4 Results

4.1 Effects of disk gravity

We conducted our first suite of numerical runs with the tools described above, four or five giant planets and 30,000 massless planetesimals initially distributed among planetary orbits. In this first set of simulations we included only the effect of disk gravitational field, disregarding drag produced by the gas. We used disk models with vertical exponential profile described in Sect. 2.2 and assumed constant scale height $z_0 = 0.05$ au (therefore $\beta = 0$). The surface density at 1 au was $\Sigma_0 = 2000$ g/cm^2, and we tested two density profiles: (i) steeper with a canonical exponent $\alpha = -1.5$, and (ii) shallower with an exponent $\alpha = -1$. We chose the inner disk radius to $R_i = 1$ au heliocentric distance and varied the outer disk radius R_o from 30 au to 100 au. With these parameters, we can use Eq. (10) to compute the total disk mass M. For our models, it ranged from about a percent to nearly 14 percents of the solar mass (see Table 1). Note that models for which M exceeds ten percent of the solar mass are at danger of directly fragmenting into giant planets or sub-dwarfs via Toomre instability, but we do not investigate this issue. Here, we rather consider them as end-members of a parameter spectrum for models we investigate. In all cases, we consider an exponential decay of the gas density with a timescale of 2 Myr. Note that this timescale is initially longer than a characteristic timescale of secular eccentricity and inclination oscillations of planetesimal orbits induced by the disk gravity. As the total mass of nebula decreases though, the two timescales may become comparable (see examples below).

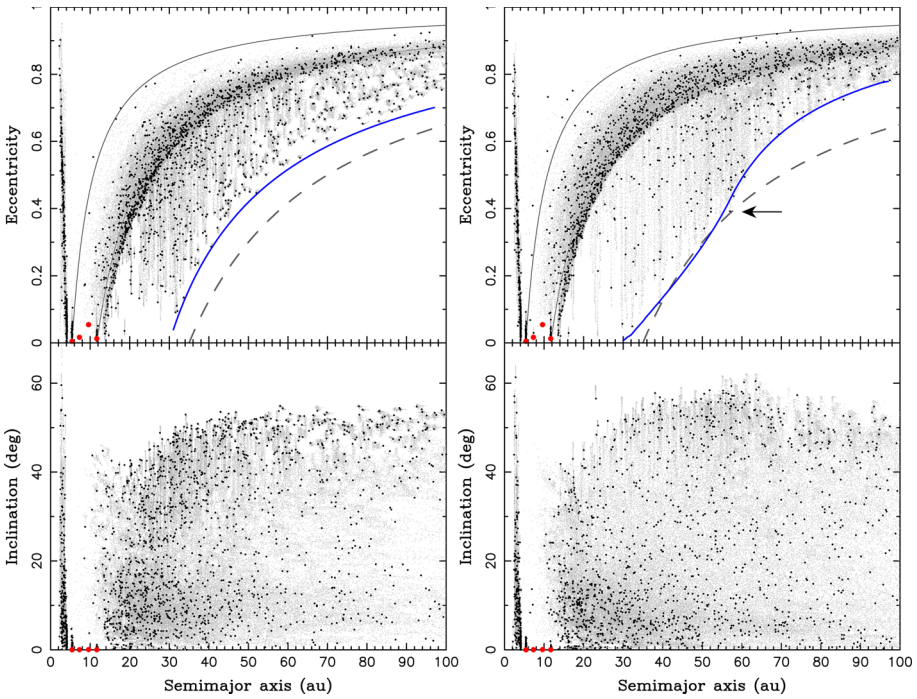

Fig. 5 Heliocentric orbital elements of planets (red symbols) and planetesimals (black symbols) at the end of our runs (time 10 Myr). Top panels show semimajor axis versus eccentricity; bottom panels show semimajor axis versus inclination. Left panels used disk with an outer radius $R_o = 30$ au, and right panels had $R_o = 100$ au; in both cases, we used shallower density profile with $\alpha = -1$. Gray symbols are tracks of the shown planetesimals in the last 2 Myr of the simulation. Dark gray and solid lines in the upper panels are perihelion lines at Jupiter and Neptune (innermost and outermost planets), dark gray and dashed line delimits orbits with perihelion of 35 au. Blue lines are theoretical limits to which planetesimals are expected to decouple from planetary influence by the secular effects of disk gravity at 40° inclination (see the text for more details) The arrow on the top and right panel indicates position of a particle, whose orbital evolution is shown in Fig. 8

4.1.1 Four-planet simulations

We first consider the simulations with four giant planets. Here we present results of runs with shallower density profile, $\alpha = -1$, but we note that results with the canonical value, $\alpha = -1.5$, are qualitatively the same. Figure 5 shows orbital elements of planets and planetesimals for two extreme disk choices, $R_o = 30$ au (left) and $R_o = 100$ au (right), and at the end of our simulations, time 10 Myr. In both cases, number of simulated planetesimals considerably dropped, to $\simeq 3$–5% of the initial populations. This is understood, because their initial locations in between the planetary orbits make them highly unstable. Very quickly, particles undergo scattering encounters with planets which eject them in a random fashion along the planets' Tisserand tails. As a result, at 10 Myr basically no planetesimal has semimajor axis value in between the planets and those which still keep interacting with the planets by short-range encounters have perihelia q mostly reaching less-massive ice giants, Uranus or Neptune. The zone characterized by q in between Jupiter and Neptune semimajor axes (see top panels of Fig. 5) is thus the main avenue along which the planetesimal orbits evolved, many toward large a to become eliminated from our simulation. In the same time,

planetary encounters have also the capability to lift orbital inclinations of the planetesimals up to $\simeq 30°$ to 35°.

The presence of the disk gravitation adds a new element to the above outlined story. In a secular approximation (often also called Kozai integrable approximation, e.g., Chap. 8.2 in Morbidelli 2002), when the mean anomaly is eliminated from Hamiltonian, the problem accounting for the solar and disk gravitational effects reduces to two degrees of freedom with only eccentricity e and argument of perihelion ω remaining active variables. This is because at this level: (i) the semimajor axis a is conserved, (ii) axial symmetry of the potential implies that the inclination I evolves in a correlated way with the eccentricity via a conserved parameter $\cos I\sqrt{1-e^2} = c$ (and longitude of node may be obtained via formal quadrature). Additionally, the transformed disk potential remains constant; in the simplest, first-order theory this is just the orbit-averaged potential $\bar{\Phi} = C$ (averaging computed along a fixed elliptic orbit). Therefore isolines of constant C in the (e, ω) space represent evolutionary tracks due to disk perturbation.

As the orbits follow these tracks, eccentricity may undergo large oscillations when c is sufficiently small (orbits having initially high inclination and/or high eccentricity). As a result, the perihelion of a planetesimal orbit may decouple from planets (becoming larger than heliocentric distance of Neptune), and undergo oscillations conserving semimajor axis. This is observed for some of the particle orbits at the top panels of Fig. 5. Obviously, after completing one secular cycle, the particle orbit returns back to the perihelion zone reachable by the planets. If it avoids very close encounter with a planet, it may eventually continue its secular evolution due to the disk gravity. (Note this is exactly the type of evolution cometary orbits undergo also at much larger heliocentric distances, where the disk gravity role is replaced by the galactic tidal field, e.g., Higuchi et al. 2007.) The secular-cycle period is inversely proportional to the disk density. So as the nebula disperses, some of the planetesimal orbits may asymptotically remain in the state of a high perihelion decoupled from planets. If this value is high enough (say larger than $\simeq$35–37 au), as found in some cases by Kretke et al. (2012), it may leave a population of TNOs on such orbits till the present epoch. If the TNOs with such orbits are excluded by existing observations, the corresponding disk model could be invalidated.

So the question reduces to finding the maximum perihelion distance (or minimum eccentricity) a particle orbit may reach during such secular cycles for a given semimajor axis value and a chosen disk model. The relevant portrait of $\bar{\Phi} = C$ isolines in the (e, ω) plane may be computed numerically. (Note that thanks to mirror symmetry about the disk midplane at $z = 0$, the secular orbital evolution is symmetric about $\omega = 180°$ and we can restrict to the ω values in between 0° and 180°.) To do that one needs to select the disk parameters and two constants: (i) semimajor axis a, and (ii) $c = \cos I\sqrt{1-e^2}$. The former is obvious, and the latter requires some reference initial conditions. Figure 6 shows a sample of such phase portraits for the disk model used in the left panels of Fig. 5. This corresponds to a smaller disk with $R_o = 30$ au and shallow density profile $\alpha = -1$. The reference initial orbit had inclination 40° (note the planetesimal orbits decouple from the direct scattering regime by planets when having typically an inclination value between 35° and 40°) and perihelion 12 au (representing an extreme example of orbits scattered on planets into their Tisserand channel), and we chose two examples of semimajor axis (i) $a = 30$ au (left), and (ii) $a = 50$ au (right). Depending on the initial (unconstrained) value of ω, the orbits may follow some of the $C =$ const. trajectories seen in Fig. 6. For instance, orbits with $a \simeq 30$ au start at eccentricity of $\simeq 0.6$ and, according to the left panel of Fig. 6, they can either stay oscillating with large values of eccentricity, or—for ω value near 90°—they can evolve to very low eccentricities. Indeed, this is seen in Fig. 5 (left and top) where some particles decouple from planets at

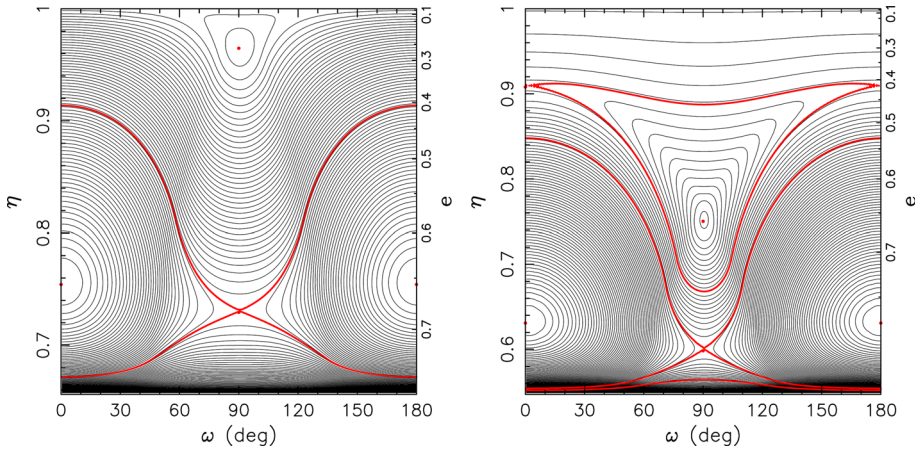

Fig. 6 Secular evolutionary tracks due to the disk gravity: isolines of a constant value of the orbit-averaged perturbing potential—$\bar{\Phi} = C$—in the plane defined by the argument of perihelion ω (abscissa) and eccentricity e (right ordinate; left ordinate shows $\eta = \sqrt{1-e^2}$). Portraits correspond to the disk model at the left panels of Fig. 5, namely outer disk radius at $R_\mathrm{o} = 30$ au. Left panel for semimajor axis $a = 30$ au, right panel for $a = 50$ au. The constant $c = \cos I\sqrt{1-e^2}$ has been chosen for initial value $I = 40°$ and perihelion distance 12 au (corresponding to Neptune's heliocentric distance). Red symbols are stationary points of the secular model, and red lines are separatrixes associated with the secularly unstable solutions

$a \simeq 30$ au and evolve to $e < 0.1$. Similarly, when $a = 50$ au and the initial eccentricity corresponds to $\simeq 0.75$, the right panel of Fig. 6 indicates that secular evolution may drive orbits to various eccentricity values. However, in this case, the $e \lesssim 0.4$ region is excluded. This is because for low-eccentricity orbits with inclinations up to 40° the orbital evolution is characterized by only steady circulation of ω about a stable center. This region is not connected to high-eccentricity zone. (Occurrence of this unperturbed low-eccentricity zone is known for a long time from analysis of Kozai dynamics exterior to planets, e.g., Morbidelli 2002, Chap. 8.2.) Again, a quick look at Fig. 5 (left and top) confirms that planetesimal orbits that eventually decoupled from the influence of planets at $a \simeq 50$ au evolve their eccentricity to the lowest value of about 0.4. We completed similar analysis for various values of a in between 30 au and 100 au and each time determined the lowest eccentricity value connected by the secular evolution with the assumed initial high-eccentricity state. (Note this value is well approximated by the eccentricity state of the unstable equilibrium of the secular model at $\omega = 0°$, see the right panel of Fig. 6.) The resulting barrier for secular evolution due to the disk gravity is shown by the blue curve in Fig. 5 (left panel; in this case, it is close to $q \simeq 30$ au value). There is an excellent agreement between this limit and the lowest eccentricity values attained by the planetesimals during their secular evolution for all tested values of a. This consistency helps verifying that the disk gravity was correctly implemented in the `swift` code.

The above outlined analysis needs to be redone when changing some of the disk parameters. For instance, taking the outer disk boundary at $R_\mathrm{o} = 100$ au, and keeping $\alpha = -1$, there is no self-similarity, by which the previous results could be recalibrated. Indeed, the phase portraits $\bar{\Phi} = C$ look now different. Figure 7 shows two examples for (i) $a = 50$ au (left), and (ii) $a = 75$ au (right). At $a = 50$ au, the secular evolution is dominated by libration about the stable stationary point at $\omega = 90°$, with an unstable point at $\omega = 0°$. Initial eccentricity of $\simeq 0.6$ may now evolve to eccentricities as small as $\simeq 0.3$. At larger heliocentric distances,

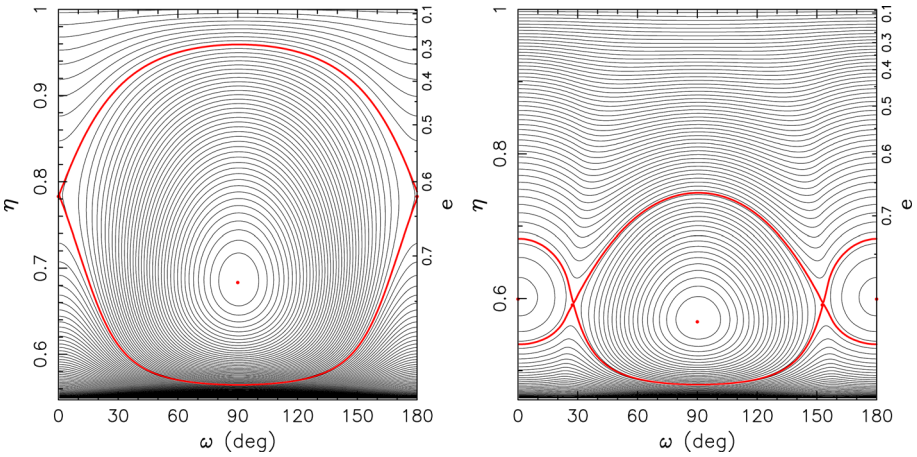

Fig. 7 The same as in Fig. 6, but now for the disk model corresponding to simulation in the right panels of Fig. 5, namely outer disk radius at $R_o = 100$ au. Left panel for semimajor axis $a = 50$ au, right panel for $a = 75$ au

such as $a = 75$ au on the right panel of Fig. 7, the libration zone shrinks. Additionally, the unstable points move to nonzero ω values and new stable points arise at $\omega = 0°$ (or $\omega = 180°$). Orbits initially having $e \simeq 0.75$ now secularly connect to minimum eccentricity of $\simeq 0.68$. We again performed similar analysis of the secular phase portraits $\bar{\Phi} = C$ for all values of semimajor axis a and obtained limiting eccentricity value reachable from the planet-crossing channel. This is shown by the blue curve on the top and right panel of Fig. 5. Again, there is an excellent agreement between this limit and minimum eccentricities attained by particles in our numerical simulation. The limiting curve in the (a, e) plane has now more complex geometry, not corresponding to a single value of perihelion, but we note that the largest perihelia reached have about 35 au (gray and dashed curve in Fig. 5). It is interesting to observe that at $a \simeq 90$ au (say), the planetesimal orbits in the smaller-disk model with $R_o = 30$ au decouple to larger perihelion than in the larger-disk model with $R_o = 100$ au (top panels of Fig. 7). While slightly counter-intuitive, this result is simply dictated by the respective secular approximation, in particular location of critical points and separatrixes for the chosen parameters a and c.

In order to illustrate the planetesimal dynamics in the two regimes, planet dominated and disk dominated, we selected one particle from the run shown on the right panels of Fig. 5 (see the arrow). Figure 8 shows its heliocentric orbital elements through our 10 Myr simulation. Up to about 3 Myr, the particle evolves primarily under the effects of planets. Close encounters with them make all orbital elements evolve in a random-walk fashion, with semimajor axis having even an excursion briefly beyond 150 au in the proto-scattering disk of planets. Starting from about 3 Myr, the orbital evolution switches into a disk-dominated, secular regime. Perihelion stays in the Neptune zone only, and the perturbations of the semimajor axis are much smaller. Additionally, there are periods when eccentricity decreases enough to save the orbit from the reach of planets, with correlated oscillations of the inclination. The period of these secular oscillations increases as the nebula disperses and becomes longer than a Myr at the end of our simulation. The argument of perihelion ω oscillates in between $\simeq 200°$ and $\simeq 340°$, notably in the mirror zone to that seen on the left panel of Fig. 7. Location near the separatrix emerging from the unstable secular equilibria at $\omega = 180°$ and $\omega = 360°$ triggers the large and regular eccentricity oscillations.

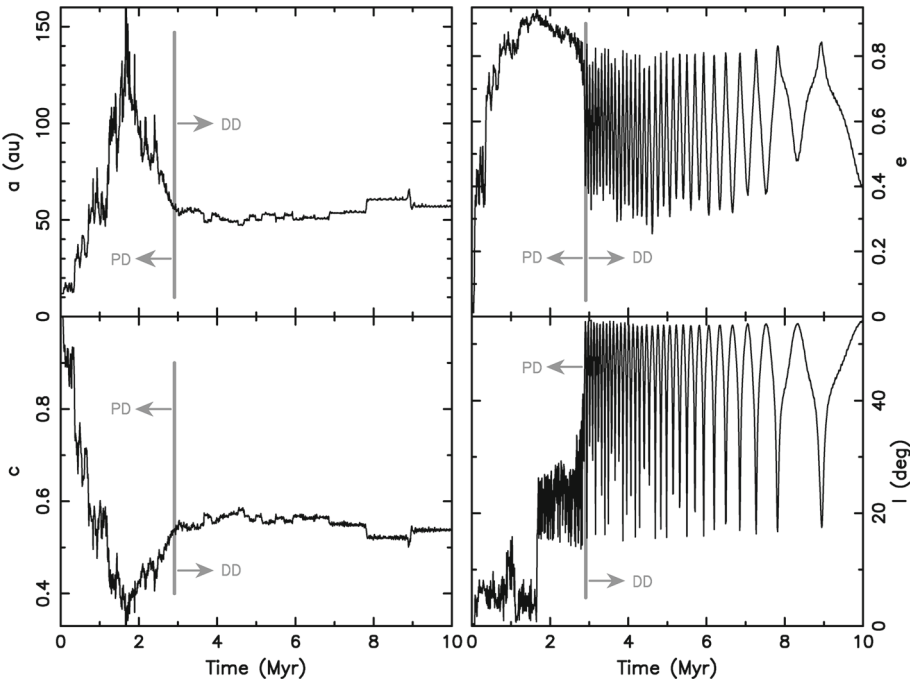

Fig. 8 An example of a planetesimal orbit evolution from a simulation shown in Fig. 5, right panels ($R_o = 100$ au, $\alpha = -1$): (i) semimajor axis a (left and top), (ii) eccentricity e (right and top), (iii) inclination I (right and bottom), and (iv) secular invariant $c = \cos I\sqrt{1-e^2}$ (left and bottom). From $\simeq 3$ Myr, the particle is only weakly interacting with the outer planets (Uranus and Neptune), while experiencing Kozai-type secular cycles due to the disk gravity (during this phase the argument of perihelion ω librates in a restricted zone between $\simeq 200°$ and $\simeq 340°$). As the mass of the disk decays, their period increases. The gray line indicates the transition moment, labels PD and DD stand for planet- and disk-dominated phases of the orbital evolution

We performed similar analysis of all our four-planet simulations with outer disk boundary in between 30 and 100 au and two indexes of density profile ($\alpha = -1$ and -1.5; see data in Table 1). We were mainly interested in estimating the maximum perihelia to which the planetesimals can decouple from the planets in our simulations. Curiously, we never found cases of particles with maximum perihelia larger than seen in Fig. 5, namely $\simeq 37$ au, based on our statistics of 30,000 propagated particles. Only in the case with $\alpha = -1$ and $R_o = 40$ au disk, the simulation ended with two decoupled particles having perihelion $\simeq 38$ au and orbital inclination $\simeq 50°$. These would be considered as extreme examples of a detached scattering disk population with slightly larger inclination than typically observed. We thus cannot fully confirm conclusions in Kretke et al. (2012), but we do not know the reason for the difference.

4.1.2 Five-planet simulations

Next, we discuss results of simulations containing five giant planets. We still consider gravitational effects of the protoplanetary disk only (no drag), and we use the same set of models as in Sect. 4.1.1. This means a suite of disks with outer boundary in between $R_o = 30$ au and $R_o = 100$ au, and we probe two power-law profiles of the surface density with $\alpha = -1$ and $\alpha = -1.5$.

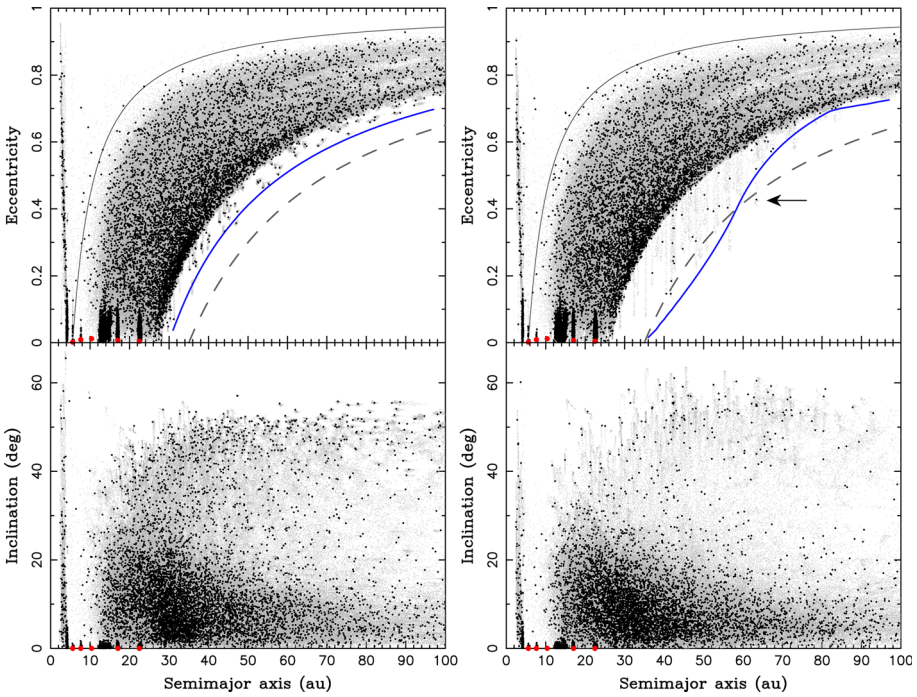

Fig. 9 The same as in Fig. 5, but now for the initial configuration with five giant planets (see Sect. 3.2; left panels used disk with an outer radius $R_o = 30$ au, right panels had $R_o = 100$ au, in both cases we used shallower density profile with $\alpha = -1$). The outermost ice giant, Neptune, is now at larger heliocentric distance. This makes the channel of planet dominance wider and shrinks the possibility for planetesimals to decouple from the reach of the planets. Blue lines again from the analysis of the secular phase flow of the corresponding disk model. The arrow on the top and right panel indicates position of a particle, whose orbital evolution is shown in Fig. 10

Figure 9 shows the same information as Fig. 5, namely orbital elements of the planetesimals that remained at the end of two runs with outer disk radii bracketing the tested interval of values, $R_o = 30$ au (left) and $R_o = 100$ au (right). We also show orbital tracks of these surviving particles during the last 2 Myr of simulation (gray dots). The boundary delimited by the blue lines at the top panels originates from the analysis of the secular model, as explained in Sect. 4.1.1, but now the c parameter of the mean disk potential $\bar{\Phi}$ is defined by initial orbits having 40° inclination and 22 au perihelion (given larger heliocentric distance of Neptune in these simulations). Overall, the conclusions here are the same as in the case of four-planet jobs. Obviously, making the planetary system more extended heliocentrically, the Tisserand channel in the (a, e) plane controlled by planets is now larger. With the same disk models, this leaves less space for the decoupled planetesimals whose orbits are dominantly controlled by the disk gravity. As seen mainly in the left and top panel ($R_o = 30$ au; compare withe same panel in Fig. 5), most orbits that populate the orbital space with perihelia larger than heliocentric distance of Neptune jump into their location by scatterings on planets rather than showing regular secular evolution by the disk gravity.

These occasional scattering encounters with ice giants, now at larger heliocentric distance, may eventually launch particle orbits onto larger perihelion zone, or evolving to that zone, overcoming thus the secular barrier discussed above. For instance, the arrow on the right

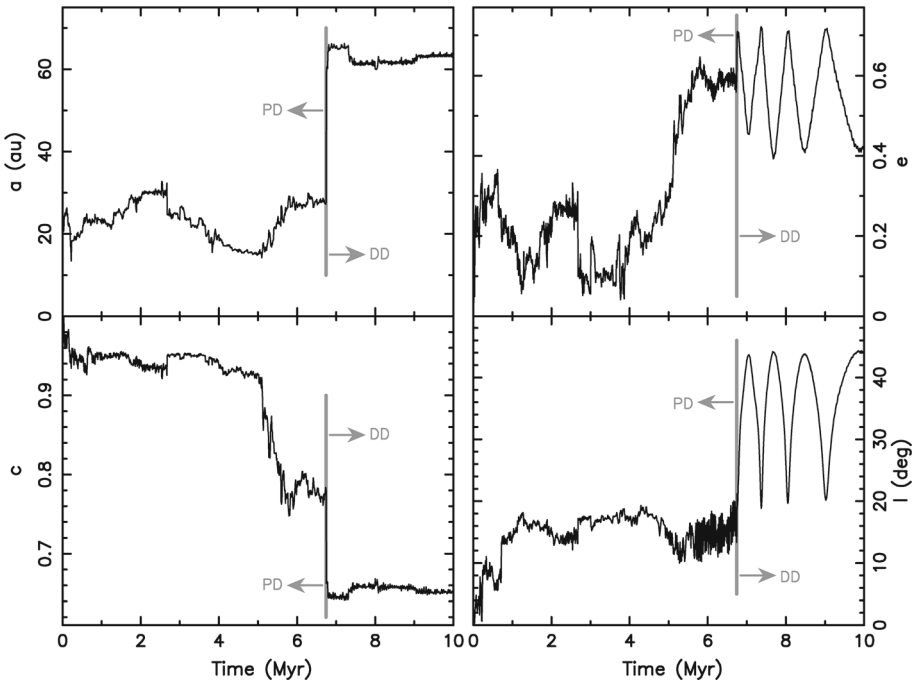

Fig. 10 An example of a planetesimal orbit evolution from a simulation shown in Fig. 9, right panels ($R_{\rm o} = 100$ au, $\alpha = -1$): (i) semimajor axis a (left and top), (ii) eccentricity e (right and top), (iii) inclination I (right and bottom), and (iv) secular invariant $c = \cos I\sqrt{1-e^2}$ (left and bottom). From $\simeq 6.7$ Myr, the particle is only weakly interacting with the outer planets (Uranus and Neptune), while experiencing Kozai-type secular cycles due to the disk gravity (during this phase the argument of perihelion ω librates in a restricted zone between $\simeq 30°$ and $\simeq 150°$). As the mass of the disk decays, their period increases. The gray line indicates the transition moment, labels PD and DD stand for planet- and disk-dominated phases of the orbital evolution

panel points to one such case, whose orbital history is shown in Fig. 10. Contrary to the case shown in Fig. 8, this particle interacts with ice giants only. This is because now the wider heliocentric zone of planets can accommodate such weakly evolving planetesimals at larger heliocentric distance. At $\simeq 6.7$ Myr, however, a close encounter with Neptune launches this particle into a disk-dominated regime secular cycles. As it starts from lower inclination, $\simeq 25°$, the c value is now larger and the blue limiting curve in Fig. 9 is slightly off (as it was computed for $c \simeq 0.55$). At later times, if the secular oscillations phase is restricted to a suitable range (about 0.1 of all possibilities), this particle may be left in a planet-decoupled state with semimajor axis of $\simeq 62$ au, eccentricity $\simeq 0.4$ and inclination $\simeq 44°$. The argument of pericenter librates between $\simeq 30°$ and $\simeq 150°$; this is because the relevant phase portrait resembles that on the left panel of Fig. 7, with only a slight shift toward smaller η, or larger e, values. Noticing in Fig. 9 that perhaps one more particle has a similar fate, we estimate $\lesssim 10^{-5}$ chance per disk planetesimal to be decoupled at distant TNO zone in this simulation. (Note we also assume that about every tenth particle shown in Fig. 10 has the right phase of the secular cycle.) Interestingly, the final orbit of this outlying particle may still be considered as a plausible tail-member of the detached scattering disk (given the maximum inclination value of $\simeq 42°$ and perihelion not exceeding $\simeq 37$ au).

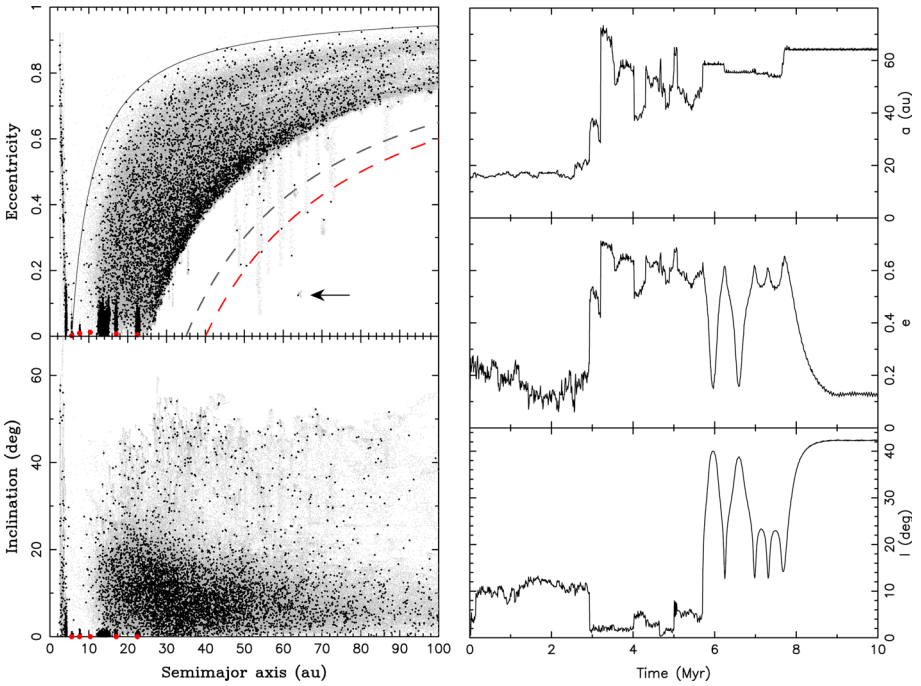

Fig. 11 Left: The same as in Fig. 9, but now for in intermediate disk with an outer radius $R_o = 60$ au (and still $\alpha = -1$). The gray dashed line at the top part indicates orbit with $q = 35$ au, and the red dashed is for $q = 40$ au. Few particles decoupled beyond this limit with the most extreme case pointed out by the arrow. Right: Orbital evolution of the particle indicated with the arrow on the left through the whole 10 Myr span of our simulation: (i) semimajor axis (top), (ii) eccentricity (middle), and (iii) inclination (bottom). Planet- to disk-dominated phases switch at $\simeq 5.7$ Myr, when Neptune scatters the particle onto an orbit with slightly large semimajor axis. The eccentricity/inclination oscillations, as well as behavior of the argument of pericenter ω, may be well understood using a Kozai secular approximation. The respective phase portraits are similar to that on right panel of Fig. 6, except for smaller inclination (implying larger c integral) make the whole structure shifted to smaller eccentricity. In the last period, time $\gtrsim 8$ Myr, the orbit slowly swings near the separatrix of the stationary point at $\omega = 90°$ and reaches small eccentricity. Largely dissipated nebula is not able to keep the secular evolution further

Few more extreme cases were observed in the simulation with $\alpha = -1$ and $R_o = 60$ au disk (see Fig. 11). Here, five particles were scattered to a similar orbital regime compatible with a tail of the detached scattering disk (all asymptotic inclination values $< 42°$). However, four had their terminal perihelia larger than 40 au, with the most extreme case pointed out with an arrow on the left panel of Fig. 11, and it orbital evolution shown on the right panel of Fig. 11. This particle was softly bouncing in the proto-scattering disk fed by ice giants in our simulation until it received a more pronounced kick in semimajor axis at about 5.7 Myr. The disk-dominated orbital phase, with characteristic Kozai cycles in eccentricity and inclination started, until it again received a further kick from Neptune at about 7.7 Myr. This event let it evolve toward a high-perihelion state with an asymptotic value of $q \simeq 55$ au and inclination about 42°. Collectively, an equivalent of about three particles got in this run decoupled beyond the zone of detached scattering disk. (Note that two of the four particles reside in this zone for only part of their secular cycle.) This implies about $3/30{,}000 = 10^{-4}$ probability to decouple to such extreme orbits. In the simulations with $R_o = 50$ au and $R_o = 80$ au an equivalent of about one particle had the same evolution, meaning about a third $\simeq 3 \times 10^{-5}$ probability

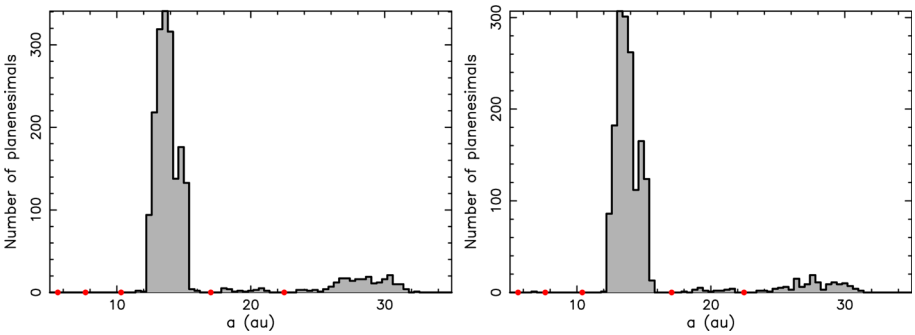

Fig. 12 Number of planetesimals at the end of our simulations in different bins of semimajor axis (abscissa) on near-circular ($e \leq 0.1$) and near-coplanar ($I \leq 5°$) orbits. The two panels correspond to simulations from Fig. 9, namely with disk boundary at $R_o = 30$ au (left) and $R_o = 100$ au (right). Red symbols denote location of planets. The largest population is located in between orbits of the first two ice giants ($\simeq 11$ to $\simeq 16$ au); beyond $\simeq 17$ au the data represent unstable orbits visiting near-circular and low-inclination orbits only temporarily

to decouple planetesimal orbits beyond the detached scattering disk. While nonzero, these values are still at least an order-of-magnitude smaller than found in Kretke et al. (2012) for comparable disk parameters.

There is a further interesting detail that warrants a comment. We note that significantly more planetesimals survived in these five-planet simulations at 10 Myr epoch (about 25%) than in the previously discussed four-planet simulations. This is because the wider spacing of planets now gives more changes to the particles to escape very close encounters to the planets. One aspect is revealed by a closer look at Fig. 9 reveals that a fair amount of particles remains on a quasi-stable orbits in between the third and fourth giant planets. This is because the assumed resonant sequence of planets in these models has 2:1 separation between these planets (as opposed to 3:2 chain elsewhere). This opens large enough gap to hold fairly stable, near-circular and near-coplanar orbits of the planetesimals in this zone. We find that about 5% of the initially distributed orbits remain at the end our simulation with semimajor axes in between 11 au and 16 au, eccentricities less than 0.1 and inclination less than 5° (Fig. 12). Apart from this peculiar population, there are also many more particles left to interact with ice giants only in the five-planet simulation. This is because many of them are in a smaller danger to directly interact with Jupiter or Saturn. More on the role of the surviving population will be discussed in the next section.

4.2 Effects of disk gravity coupled with gas drag

Previous simulations were approximate, because they did not take into account all possible effects of the nebular gas on the motion of planetesimals. In particular, the role of the gas drag has been neglected. At the first sight, it might seem to be most important in the zone inner to the giant planets, where the gas density is large enough, and less so in the outer Solar system. But this conclusion may also depend to the assumed size of the planetesimals (see, e.g., Brasser et al. 2007). We thus decided re-run some of our previous simulations with now the effects of the gas drag included. We tested 100 km, 10 km and 5 km for the planetesimal sizes, and assumed their density equal to 1 g/cm^3.

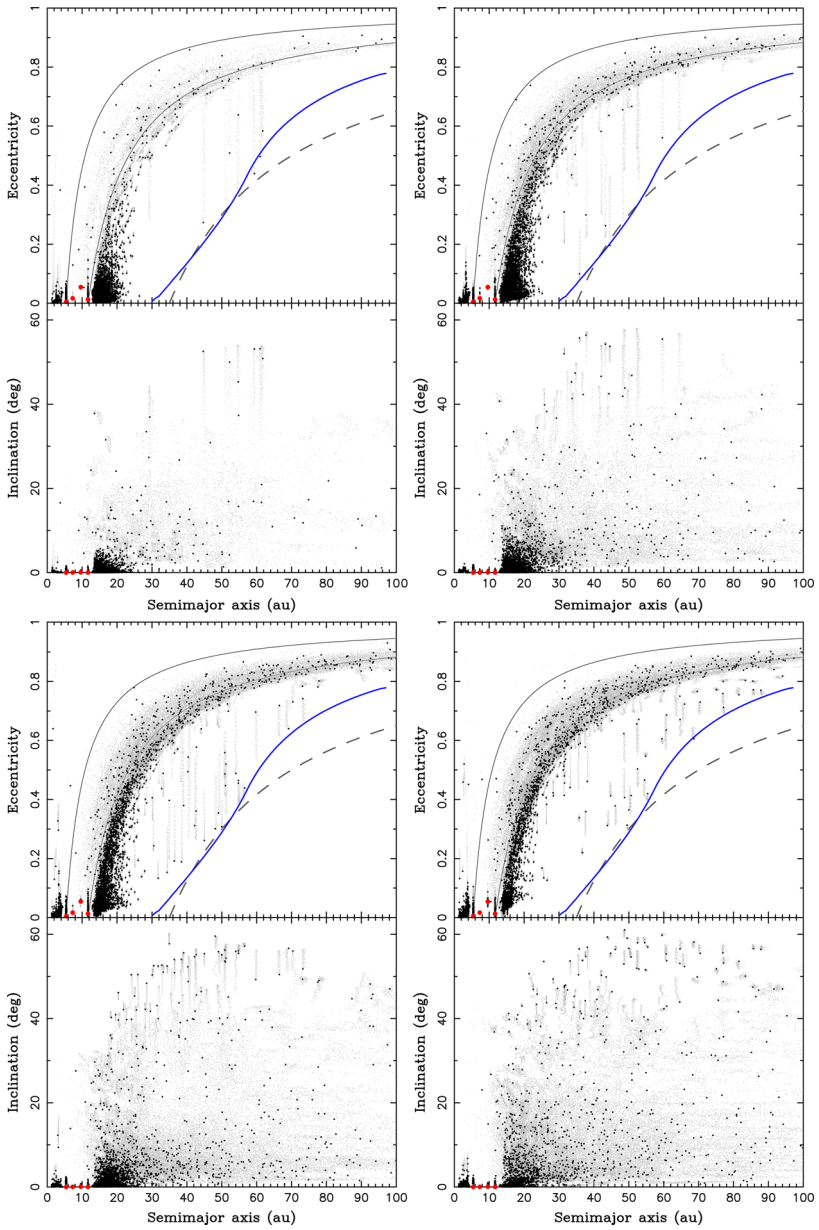

Fig. 13 Similar to Fig. 5, but now for simulations where both gravitational and drag effects of the nebular gas were taken into account. In all panels, the outer disk radius was $R_o = 100$ au ($R_i = 1$ au, $z_s = 0.05$ au, $\alpha = -1$, $\beta = 0$). Planetesimals were given $D = 100$ km size, and we assumed their bulk density of 1 g/cm^3. We varied surface density Σ_0 at 1 au heliocentric distance: (i) $\Sigma_0 = 2000$ g/cm^2 (top and left; this is the same value used in the right panel of Fig. 5, where only the gas drag was disregarded), (ii) $\Sigma_0 = 1000$ g/cm^2 (top and right), (iii) $\Sigma_0 = 500$ g/cm^2 (bottom and left), and (iv) $\Sigma_0 = 200$ g/cm^2 (bottom and right). In all cases, particles scattered by Jupiter inward quickly decouple by gas drag to the outer zone of the asteroid main belt. When density is sufficiently large (top panels), the outward scattered particles are also driven by the gas drag to orbits exterior to Neptune, some being captured in mean-motion resonances with this planet. Blue lines again from the analysis of the secular phase flow of the corresponding disk model

4.2.1 Four-planet simulations

As above, we start with the four-planet runs and $D = 100$ km planetesimals. The four panels in Fig. 13 show the projected final orbital configuration of planets and remaining planetesimals at 10 Myr for our most extended disk model ($R_o = 100$ au) and shallow surface density profile ($\alpha = -1$); therefore, they may be compared with data on the left panel of Fig. 5. From top-left to bottom-right panels, models with decreasing surface density at 1 au heliocentric distance are shown: $\Sigma_0 = 2000$ g/cm^2 to $\Sigma_0 = 200$ g/cm^2 (correspondingly, the total initial mass of the nebula decreases from about 14 to 1.4% of the solar mass). In addition to (i) the chaotic evolution of particles directly interacting with planets, and (ii) the regular evolution of particles decoupled from the planets driven by the disk gravity, we see now a third element in orbital dynamics of planetesimals decoupled from planets below about 30 au heliocentric distance. This is due to the gas drag. As discussed, for instance by Brasser et al. (2007), the aerodynamic drag results in orbital decay toward smaller semimajor axis values, accompanied with circularization and inclination decrease. As a result, especially for larger-Σ_0 models, a large number of planetesimals are stored to heliocentric zone exterior to Neptune, decoupled from planets at small eccentricity and inclination orbits.[1] This is very different from what is seen in Fig. 5 when the aerodynamics drag was neglected. Selecting a target zone delimited by orbital elements $a > 12.5$ au, $e < 0.4$ and $i < 20°$ (together with $q > 11.8$ au to approximately characterize orbits exterior to Neptune), we find there are about 6700, 4550, 2700 and 1430 particles left in the simulation from top-left to bottom-right windows in Fig. 13 (much more than 120 in the left panel of Fig. 5). [2] Recall that the initial number of propagated particles was 30,000, so this represents between 5 and 22% of particles. We also find that in the simulations with the most massive disks, $\Sigma_0 = 2000$ g/cm^2 and $\Sigma_0 = 1000$ g/cm^2 at the two top panels, some of these remaining particles are located in the exterior mean-motion resonances with Neptune (though majority is not). Overall, these particles are very interesting, because they were redistributed to sufficiently low-eccentricity and low-inclination orbits exterior to Neptune from initial orbits in between the giant planets. In the next phase of evolution of the Solar system, when planets start to radially migrate and undergo reconfiguration, these particles will contribute to populations of minor bodies doped by exterior disk as described by previous works (see Sect. 1).

We have verified that the above-mentioned results do not depend critically on the exterior radius of the planetesimal disk; in particular, running simulations for $R_o = 50$ au and $R_o = 30$ au, we again obtained a significant number of particles stored on orbits exterior to Neptune. As expected, since the aerodynamic gas drag is the principal effect that drives the planetesimals onto these stable orbits, such deposition is even faster and more efficient for smaller bodies. In Fig. 14, we show snapshots of a selected simulation with $D = 10$ km size planetesimals. In this case, we had $\Sigma_0 = 500$ g/cm^2, to moderate the drag perturbation, and other parameters as above: $R_i = 1$ au, $R_o = 100$ au, $z_s = 0.05$ au, $\alpha = -1$, and $\beta = 0$. We note the evolution proceeds quite fast. In a few millions of years, the particles reach their terminal orbits. Additionally, few planetesimals make it to large-a orbits. This is because as soon as planets scatter them to such large-a and large-e orbits in the Tisserand funnel, their

[1] In addition, orbital structure of planetesimals scattered by Jupiter onto $a < 5$ au orbits is now also very different. The effects of aerodynamics gas drag make them evolve onto low-eccentricity orbits, many embedded in the asteroidal main belt (see, e.g., Raymond and Izidoro 2017).

[2] Note there are more particles left at the end of our simulations, namely those still strongly interacting with planets. However, since the timing of giant planet instability is not exactly known (e.g., Nesvorný et al. 2018), we are not primarily interested in them. For instance, if the reconfiguration occurred at 50 Myr, many of these particles will be still eliminated by effects of close encounters with planets.

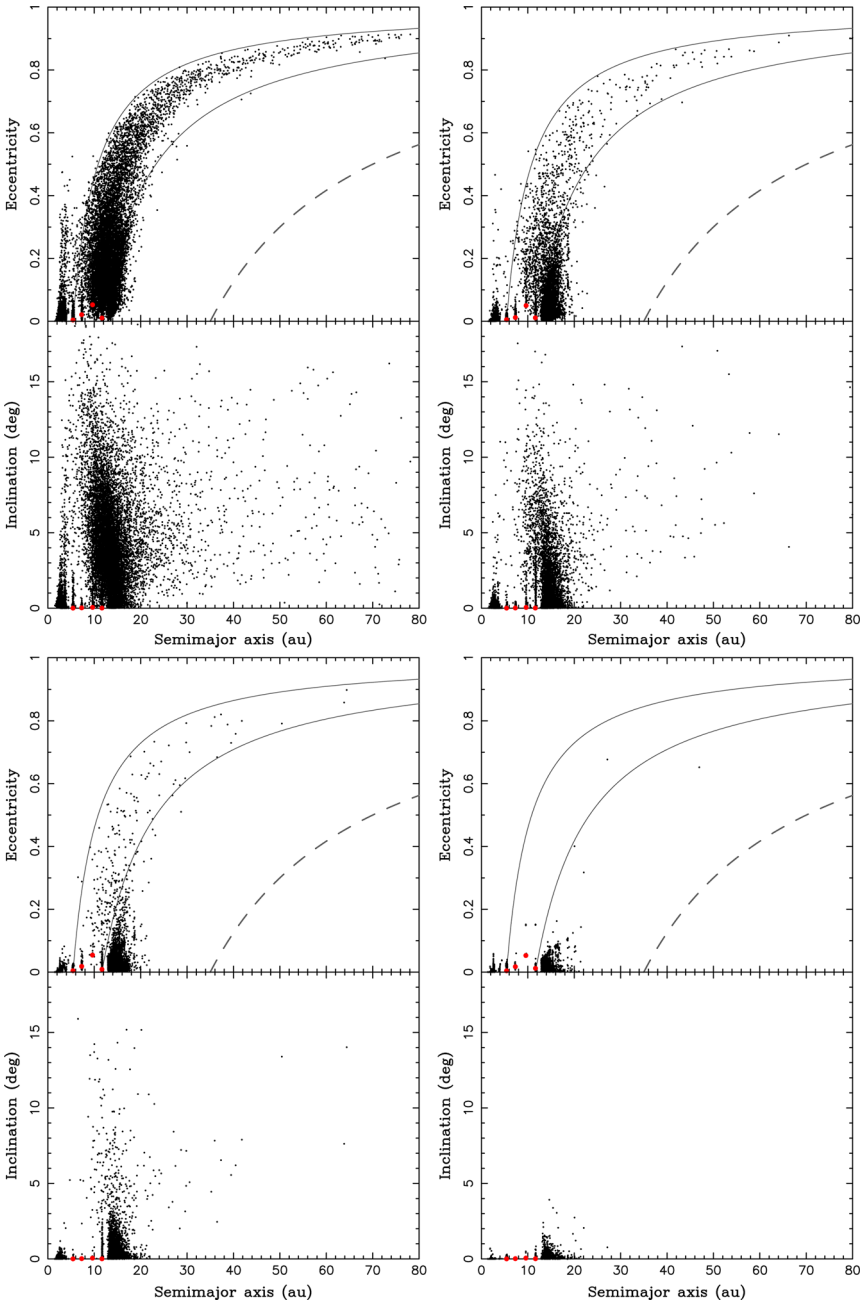

Fig. 14 Similar to Fig. 13, but here the panels show snapshots of a single simulation at different time: (i) $t = 0.1$ My (top and left), (ii) $t = 0.5$ My (top and right), (iii) $t = 1$ My (bottom and left), and (iv) $t = 5$ My (bottom and right). The outer disk radius was $R_o = 100$ au and the surface density $\Sigma_0 = 500$ g/cm^2 at 1 au heliocentric distance ($R_i = 1$ au, $z_s = 0.05$ au, $\alpha = -1$, $\beta = 0$). Planetesimals were given $D = 10$ km size, and we assumed their bulk density of 1 g/cm^3. Very few particles reach orbits with $a \gtrsim 50$ au since a strong aerodynamic gas drag quickly makes them evolve onto low-eccentricity and low-inclination orbits exterior to Neptune

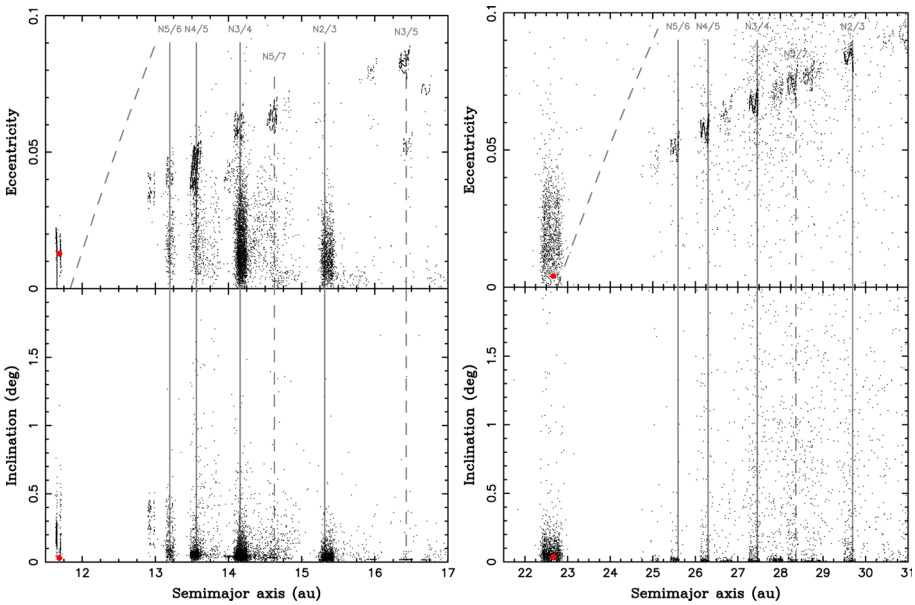

Fig. 15 Planetesimals remaining in two of our simulations at 10 Myr epoch: zoom at the heliocentric zone exterior to Neptune. Both jobs included gravitational and drag effects of the nebular gas; the left panel for model with four giant planets, right panel for model with five giant planets. The outer disk radius was $R_o = 100$ au and the surface density $\Sigma_0 = 500$ g/cm^2 at 1 au heliocentric distance ($R_i = 1$ au, $z_s = 0.05$ au, $\alpha = -1$, $\beta = 0$). Planetesimals were given $D = 10$ km size, and we assumed their bulk density of 1 g/cm^3. As already noted by Brasser et al. (2007), most of the terminal orbits are captured in exterior mean-motion resonances with planets (principally Neptune); some of the first-order resonances are highlighted with solid lines, the second-order resonances N3:5 and N5:7 with vertical dashed line. The slanted dashed line delimits orbits directly interacting with Neptune (showed with red circle)

relative velocity to the gas flow increases so much that the drag is very intense and capable of decoupling them from planetary reach. As a result, basically no small planetesimals have a chance to be scattered to the zone of a proto-Oort cloud (see, e.g., Brasser et al. 2007), but many more end now evolution just exterior to Neptune's orbit. We note there are more than 10,000 $D = 10$ km particles in Fig. 14 compared to less than 3000 $D = 100$ km particles in the bottom and left panel of Fig. 13 (corresponding to the same Σ_0 value). The inefficiency to launch small planetesimals/comets into the proto-Oort cloud has been described as a size-sorting process in Brasser et al. (2007).

Making a zoom onto the zone just exterior to Neptune at the final state of our simulation described in Fig. 14 reveals another interesting finding noted already by Brasser et al. (2007). We confirm that most of the heliocentrically distant remaining particles were located in exterior mean-motion resonances with Neptune. Left panel of Fig. 15 illustrates the situation (recall $D = 10$ km, $R_i = 1$ au, $R_o = 100$ au, $z_s = 0.05$ au, $\Sigma_0 = 500$ g/cm^2, $\alpha = -1$, $\beta = 0$). For the sake of better understanding, we show an approximate location of several first- and second-order mean-motion resonances with Neptune. Indeed, majority of particles is associated with these resonances. In contrast to the simulation for $D = 100$ km planetesimals, whose remaining orbits have eccentricity values stirred to the Neptune-crossing limit, the remaining exterior $D = 10$ km planetesimals have maximum eccentricities that stay away from this threshold. This is because they are set by the resonant capture, namely by the

stationary point of the respective resonance. Most curiously, it has been shown by Beaugè and Ferraz-Mello (1993), their Sec. 3.1, that its eccentricity value does not depend on the aerodynamic drag strength, but only by the resonance and relative velocity by which the gas molecules fall behind the local Keplerian value. The stronger drag also makes the final inclination of the remaining planetesimal orbits very small. In passing, we mention that the capture history of the particles located in the exterior mean-motion resonances with Neptune is quite rich (though it is not our intention to describe it in detail here). For instance, planetesimals residing in the N5:7 resonance were initially captured in the N2:3 resonance. Because the capture in the drag environment in temporary only, they were subsequently ejected from this resonance and later captured in the N5:7 resonance.

4.2.2 Five-planet simulations

Next, we examine five-planet runs where the effects of both disk gravity and aerodynamic drag were taken into account. We start with $D = 100$ km planetesimals. Figure 16 shows the configuration of planetesimals remaining in our runs at 10 Myr, sampling again disk models of different mass (the most massive at the top left and the least massive at the bottom right). While still existing, the effect of storing planetesimals to the orbital zone exterior to Neptune is less pronounced. This is because Neptune is now heliocentrically further, in the zone where the gas density is smaller. Nevertheless, as in the simulations discussed in Sect. 4.1.2, many planetesimals remain weakly perturbed in the heliocentric zone in between the first and second (Uranus) ice giants. Altogether, there is between 18% and 30% of planetesimals remaining in these two populations, available for further orbital evolution after planets undergo their reconfiguration.

The right panel of Fig. 15 for $D = 10$ km size planetesimals shows again that those exterior to Neptune orbit are preferentially captured in the mean-motion resonances with this planet ($R_o = 100$ au and $\Sigma_0 = 1000$ g/cm^2 in this case). Together with the zone between the first and second ice giants, there is now as many as 52% of planetesimals remaining on orbits not strongly interacting with planets.

5 Conclusions

This work may be improved in many respects. For instance, one could implement non-axisymmetric gas density distribution of the nebula consistent with the equilibrium configuration of planets, as well as abandon simplistic assumption about its truncation at some specific heliocentric distance. Modeling of a more realistic density distribution in the direction perpendicular to the planetary plane would be also desirable. Another interesting avenue to make our results more realistic is to assume the planets are not yet fully formed at the beginning of our simulations, but grow from smaller-mass cores (while also performing an initial, disc-driven migration).

While all these steps await a future research, this work provides at least a basic characteristic of an interesting population of objects that could be readily used in future numerical integrations. Namely, we show in Sect. 4.2 that some planetesimals born in the giant-planet zone may end up on low-eccentricity and low-inclination orbits exterior to Neptune at the moment when nebula dissipates. When planets set on migration and dynamical reconfiguration, prior to reaching their final orbits, these planetesimals will be dispersed by close encounters with them. Some may find their way to the long-term stable niches of minor bod-

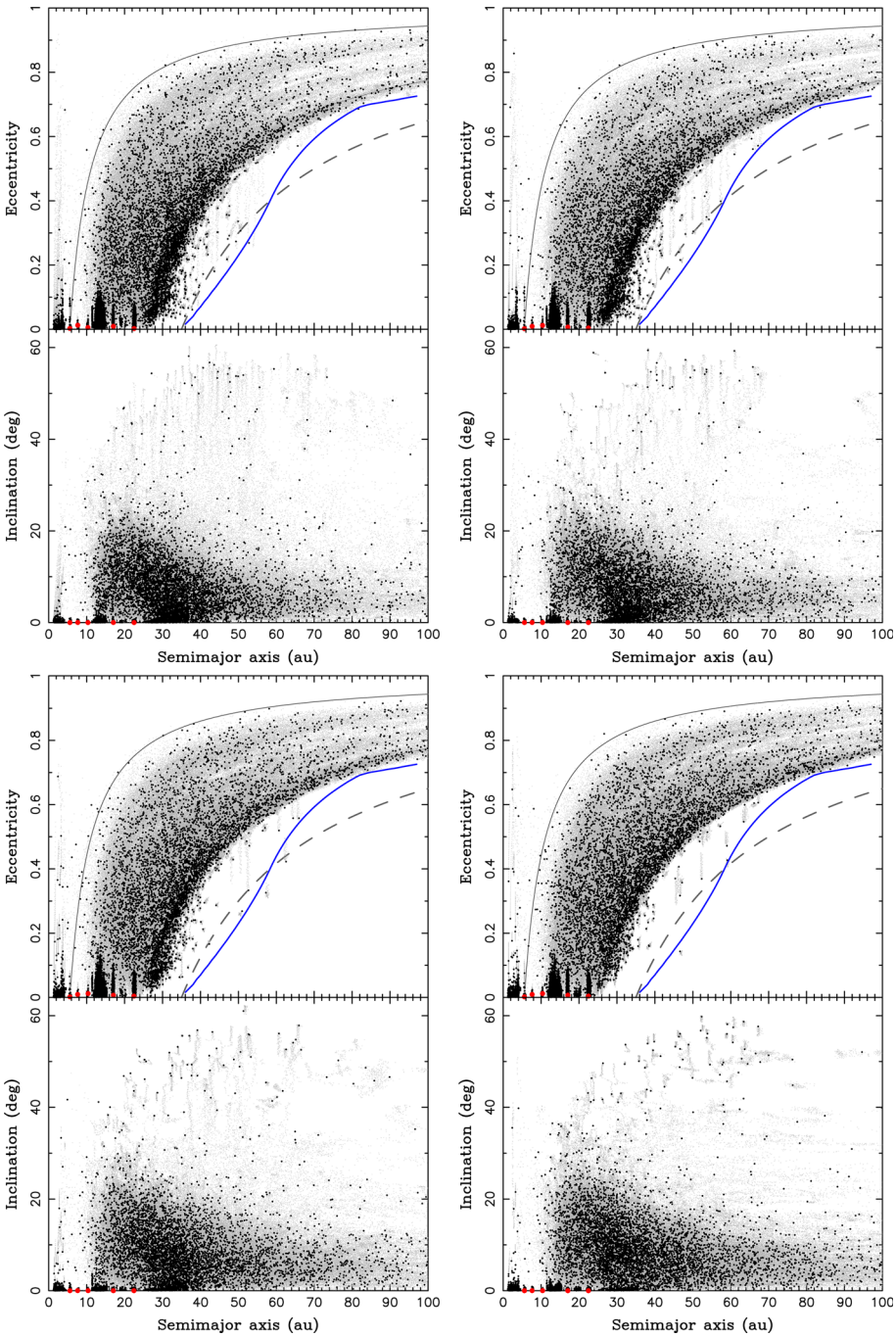

Fig. 16 Similar to Fig. 13, but now for simulations with five giant planets

ies, such as Trojans, various components of the Kuiper belt and the Oort cloud. It would be interesting to analyse their implantation probability and understand how much they can add to the previously found delivery from a population of planetesimals born at larger heliocentric distance outside the orbit of Neptune. If this contribution is significant, it may help to understand existing observations or even help resolving some pending problems. For instance, recent observation of a C-type object 2004 EW_{95} in the Plutino population by Seccull et al. (2018) is best understood if the body originally formed in the heliocentric zone delimited by giant planets and it was deposited into its current location by planetary perturbations assited by gas drag. If more such objects are found among Plutinos, and their abundance within this population is estimated by properly accounting for the observation biases, this fraction may be compared with implantation efficiency predicted by various models of planetary migration. As a second example, we may mention that current modeling indicates the population of the Oort cloud is too small to explain flux of long-period comets if built from the planetesimals in the trans-Neptunian zone (e.g., Vokrouhlický et al. 2019). Our identified population of planetesimals born among planets may help solving this problem (though another possibility would be comet contribution from free-floating planetesimals in the solar birth cluster, e.g., Levison et al. 2010).

Acknowledgements This research was supported by the Czech Science Foundation (Grant 18-06083S). We thank both anonymous referees for interesting comments that helped to improve the final form of the manuscript.

References

Alexander, R.D., Clarke, C.J., Pringle, J.E.: Photoevaporation of protoplanetary discs—II. Evolutionary models and observable properties. MNRAS **369**, 229–239 (2006). https://doi.org/10.1111/j.1365-2966.2006.10294.x. arXiv:astro-ph/0603254

Batygin, K., Brown, M.E., Betts, H.: Instability-driven dynamical evolution model of a primordially five-planet outer Solar system. Astrophys. J. Lett. **744**, L3 (2012). https://doi.org/10.1088/2041-8205/744/1/L3. arXiv:1111.3682

Beaugè, C., Ferraz-Mello, S.: Resonance trapping in the primordial solar nebula: the case of a stokes drag dissipation. Icarus **103**(2), 301–318 (1993). https://doi.org/10.1006/icar.1993.1072

Binney, J., Tremaine, S.: Galactic Dynamics, 2nd edn. Princeton University Press, Princeton (2008)

Brasser, R., Duncan, M.J., Levison, H.F.: Embedded star clusters and the formation of the Oort cloud. II. The effect of the primordial solar nebula. Icarus **191**, 413–433 (2007). https://doi.org/10.1016/j.icarus.2007.05.003

Byrd, P.F., Friedman, M.D.: Handbook of Elliptic Integrals for Engineers and Physicists. Springer, Berlin (1971)

Earn, D.J.D.: Potential-density basis sets for galactic disks. Astrophys. J. **465**, 91–95 (1996). https://doi.org/10.1086/177404. arXiv:astro-ph/9601101

Hayashi, C.: Structure of the solar nebula, growth and decay of magnetic fields and effects of magnetic and turbulent viscosities on the nebula. Prog. Theor. Phys. Suppl. **70**, 35–53 (1981). https://doi.org/10.1143/PTPS.70.35

Hayashi, C., Nakazawa, K., Nakagawa, Y.: Formation of the Solar system. In: Black, D.C., Matthews, M.S. (eds.) Protostars and Planets II, pp. 1100–1153. University of Arizona Press, Tucson (1985)

Higuchi, A., Kokubo, E., Kinoshita, H., Mukai, T.: Orbital evolution of planetesimals due to the galactic tide: formation of the comet cloud. Astron. J. **134**, 1693–1706 (2007). https://doi.org/10.1086/521815

Kretke, K.A., Levison, H.F., Buie, M.W., Morbidelli, A.: A method to constrain the size of the protosolar nebula. Astron. J. **143**, 91 (2012). https://doi.org/10.1088/0004-6256/143/4/91. arXiv:1202.2343

Kuzmin, G.G.: A model of a steady-state Galaxy which allows a velocity ellipsoid with three unequal axes. Astronomicheskii Zhurnal **33**, 27 (1956)

Lass, H., Blitzer, L.: The gravitational potential due to uniform disks and rings. Celest. Mech. **30**, 225–228 (1983). https://doi.org/10.1007/BF01232189

Lemaitre, A., Dubru, P.: Secular resonances in the primitive solar nebula. Celest. Mech. Dyn. Astron. **52**, 57–78 (1991). https://doi.org/10.1007/BF00048587

Levison, H.F., Duncan, M.J., Brasser, R., Kaufmann, D.E.: Capture of the Sun's Oort cloud from stars in its birth cluster. Science **329**, 187–190 (2010). https://doi.org/10.1126/science.1187535

Masset, F., Snellgrove, M.: Reversing type II migration: resonance trapping of a lighter giant protoplanet. MNRAS **320**, L55–L59 (2001). https://doi.org/10.1046/j.1365-8711.2001.04159.x. arXiv:astro-ph/0003421

Morbidelli, A.: Modern Celestial Mechanics: Dynamics in the Solar System. Taylor & Francis, London (2002)

Morbidelli, A., Tsiganis, K., Crida, A., Levison, H.F., Gomes, R.: Dynamics of the giant planets of the Solar system in the gaseous protoplanetary disk and their relationship to the current orbital architecture. Astron. J. **134**, 1790–1798 (2007). https://doi.org/10.1086/521705. arXiv:0706.1713

Nesvorný, D.: Young Solar system's fifth giant planet? Astrophys. J. Lett. **742**, L22 (2011). https://doi.org/10.1088/2041-8205/742/2/L22. arXiv:1109.2949

Nesvorný, D.: Dynamical evolution of the early Solar system. Annu. Rev. Astron. Astrophys. **56**, 137–174 (2018). https://doi.org/10.1146/annurev-astro-081817-052028

Nesvorný, D., Morbidelli, A.: Statistical study of the early solar system's instability with four, five, and six giant planets. Astron. J. **144**, 117 (2012). https://doi.org/10.1088/0004-6256/144/4/117. arXiv:1208.2957

Nesvorný, D., Vokrouhlický, D., Bottke, W.F., Levison, H.F.: Evidence for very early migration of the solar system planets from the Patroclus–Menoetius binary Jupiter Trojan. Nat. Astron. **2**, 878–882 (2018). https://doi.org/10.1038/s41550-018-0564-3

Press, W.H., Teukolsky, S.A., Vetterling, W.T., Flannery, B.P.: Numerical Recipes: The Art of Scientific Computing. Cambridge University Press, Cambridge (2007)

Raymond, S.N., Izidoro, A.: Origin of water in the inner Solar system: planetesimals scattered inward during Jupiter and Saturn's rapid gas accretion. Icarus **297**, 134–148 (2017). https://doi.org/10.1016/j.icarus.2017.06.030

Roig, F., Nesvorný, D.: The evolution of asteroids in the jumping-Jupiter migration model. Astron. J. **150**(6), 186 (2015). https://doi.org/10.1088/0004-6256/150/6/186

Seccull, T., Fraser, W.C., Puzia, T.H., Brown, M.E., Schönebeck, F.: 2004 EW_{95}: a Phyllosilicate-bearing Carbonaceous Asteroid in the Kuiper Belt. Astrophys. J. Lett. **855**, L26 (2018). https://doi.org/10.3847/2041-8213/aab3dc

Vokrouhlický, D., Karas, V.: Stellar dynamics in a galactic centre surrounded by a massive accretion disc—I. Newtonian description. MNRAS **298**, 53–66 (1998). https://doi.org/10.1046/j.1365-8711.1998.01564.x. arXiv:astro-ph/9805011

Vokrouhlický, D., Nesvorný, D., Dones, L.: Origin and evolution of long-period comets. Astron. J. **157**, 181 (2019). https://doi.org/10.3847/1538-3881/ab13aa. arXiv:1904.00728

Walsh, K.J., Morbidelli, A., Raymond, S.N., O'Brien, D.P., Mandell, A.M.: A low mass for Mars from Jupiter's early gas-driven migration. Nature **475**(7355), 206–209 (2011). https://doi.org/10.1038/nature10201. arXiv:1201.5177

Weidenschilling, S.J.: The distribution of mass in the planetary system and solar nebula. Astropys. Space Sci. **51**, 153–158 (1977a). https://doi.org/10.1007/BF00642464

Weidenschilling, S.J.: Aerodynamics of solid bodies in the solar nebula. MNRAS **180**, 57–70 (1977b). https://doi.org/10.1093/mnras/180.1.57

Wisdom, J., Holman, M.: Symplectic maps for the n-body problem. Astron. J. **102**, 1528–1538 (1991). https://doi.org/10.1086/115978